



The world-class Nanling metallogenic belt (Jiangxi, China): W and Sn deposition at 160 Ma followed by 30 m.y. of hydrothermal metal redistribution

Hélène Legros, Matthieu Harlaux, Julien Mercadier, Rolf Romer, Marc Poujol, Alfredo Camacho, Christian Marignac, Michel Cuney, Ru-Cheng Wang, Nicolas Charles, et al.

► To cite this version:

Hélène Legros, Matthieu Harlaux, Julien Mercadier, Rolf Romer, Marc Poujol, et al.. The world-class Nanling metallogenic belt (Jiangxi, China): W and Sn deposition at 160 Ma followed by 30 m.y. of hydrothermal metal redistribution. Ore Geology Reviews, 2020, 117, pp.103302. 10.1016/j.oregeorev.2019.103302 . insu-02428580

HAL Id: insu-02428580

<https://insu.hal.science/insu-02428580>

Submitted on 21 Jul 2022

HAL is a multi-disciplinary open access archive for the deposit and dissemination of scientific research documents, whether they are published or not. The documents may come from teaching and research institutions in France or abroad, or from public or private research centers.

L'archive ouverte pluridisciplinaire **HAL**, est destinée au dépôt et à la diffusion de documents scientifiques de niveau recherche, publiés ou non, émanant des établissements d'enseignement et de recherche français ou étrangers, des laboratoires publics ou privés.



Distributed under a Creative Commons Attribution - NonCommercial 4.0 International License

Revision 2

The world-class Nanling metallogenic belt (Jiangxi, China): W and Sn deposition at 160 Ma followed by 30 m.y. of hydrothermal metal redistribution

Hélène Legros ^{a,b,*}, Matthieu Harlaux ^{a,c}, Julien Mercadier ^a, Rolf L. Romer ^d, Marc Poujol ^e, Alfredo Camacho ^f, Christian Marignac ^a, Michel Cuney ^a, Ru-Cheng Wang ^g, Nicolas Charles ^b, Marc-Yves Lespinasse ^a

^a *Université de Lorraine, CNRS, CREGU, GeoRessources, Boulevard des Aiguillettes B.P. 70239, F-54506 Vandoeuvre-lès-Nancy, France*

^b *BRGM-French Geological Survey, 3, Av. Claude Guillemin, BP 36009, 45060 Orléans Cedex 2, France*

^c *Department of Earth Sciences, University of Geneva, 1205 Geneva, Switzerland*

^d *GFZ German Research Centre for Geosciences, Telegrafenberg, 14473 Potsdam, Germany*

^e *Univ Rennes, CNRS, Géosciences Rennes - UMR 6118, F-35000 Rennes, France*

^f *Department of Geological Sciences, University of Manitoba, Winnipeg, Manitoba R3T 2N2, Canada*

^g *State Key Laboratory for Mineral Deposits Research, School of Earth Sciences and Engineering, Nanjing University, Xianlin University Town, Nanjing 210046- China*

* Department of Earth and Atmospheric Sciences, University of Alberta, Edmonton, Alberta T6G 2E3 Canada
Mail : hlegros@ualberta.ca

Abstract

The W-Sn Maoping deposit and related W-Sn deposits from the world-class Nanling Range in Southeast China formed at ca. 160 Ma and experienced several phases of metal addition and metal redistribution between 160 and 130 Ma. Isotopic dating of ore mineral (wolframite) of Maoping demonstrates that W was deposited first, during a hydrothermal event at ca. 160 Ma. Successive fluid episodes, at ca. 156 Ma (Mo and Sn-rich fluid) and 152 Ma (REE-rich fluid), resulted in the formation of REE- and Fe-Cu-Zn-sulfide minerals. A last fluid event occurring at ca. 130 Ma was responsible for the deposition of Zr-REE-Nb-Ta minerals that are attributed to magmatic fluids derived from unexposed magmatic bodies. The three episodes of fluid circulation post-dating W deposition resulted in partial to complete resetting of the isotopic systems (mica, wolframite, xenotime), which are conventionally used for dating such deposits. We show that W and Sn mineralization in the Nanling Range formed during a unique fluid event at ca. 160 Ma. Later fluid episodes redistributed the previously deposited metals and sequentially introduced additional metals, including Mo-Sn, Fe-Cu-Zn, and Zr-REE-Nb-Ta. Direct dating of paragenetically well-constrained minerals is therefore critical for determining the age and the duration of mineralizing processes and for characterizing the fluid evolution of magmatic-hydrothermal systems, as exemplified in the Nanling Range.

Keywords

Maoping deposit - U-Pb dating - Ar-Ar dating – mica - wolframite – xenotime - tungsten deposit – Nanling Range

1. Introduction

The Nanling Range is the world's richest metallogenic belt for tungsten and tin resources with reserves of 1.7 and 1.2 million tons, respectively (e.g., Peng *et al.*, 2006; Mao *et al.*, 2011; Wang *et al.*, 2016). Recent studies have addressed the formation age of W-Sn deposits in this belt, in some cases using recently developed *in situ* dating methods such as U-Pb on wolframite (Deng *et al.*, 2019), U-Pb on cassiterite (Zhang *et al.*, 2017) and U-Pb on hydrothermal zircons (Wang *et al.*, 2016). Most Mesozoic W-Sn deposits in the Nanling range formed between 160 Ma and 150 Ma, based on U-Pb ages of cassiterite and wolframite, Ar-Ar ages on mica and Re-Os ages on molybdenite (e.g., Bai *et al.*, 2011; Feng *et al.*, 2011; Zhang *et al.*, 2015, 2017; Deng *et al.*, 2019). However, younger ages have also been reported, ranging from 160 to 130 Ma, according to mica Ar-Ar dating from several W-Sn deposits in the Nanling Range (e.g., Liu *et al.*, 2008; Chen *et al.*, 2009; Zhang *et al.*, 2009; Wang *et al.*, 2010a; Bai *et al.*, 2013). Five deposits yielded ca. 130 Ma U-Pb ages obtained on hydrothermal zircon considered to be co-genetic with tungsten mineralization (Wang *et al.*, 2016), whereas late-stage wolframite from the Wutong deposit yielded U-Pb ages ranging from ca. 104 to 92 Ma (Lecumberri-Sanchez *et al.*, 2014).

Fluid inclusion studies on W-Sn deposits from the Nanling Range indicate that gangue and ore minerals recorded multiple episodes of fluid flow of different origin, reflecting temporally and genetically decoupled fluid histories (Wei *et al.*, 2012; Ni *et al.*, 2015; Legros *et al.*, 2019). Moreover, detailed mineralogical and geochemical studies of Fe-Li-mica and fluid inclusions on the world-class Maoping and Piaotang W-Sn deposits suggest that at least four types of fluids were involved to variable extent in the formation of these deposits and provided different metals through time (Legros *et al.*, 2016, 2018, 2019). These results confirm earlier findings reporting successive hydrothermal events for the formation of peri-

granitic W-Sn deposits worldwide, but they also suggest that current genetic models for the W-Sn deposits from the Nanling Range do not properly explain their complex fluid evolution (e.g., Xi *et al.*, 2008; Feng *et al.*, 2012; Wei *et al.*, 2012; Gong *et al.*, 2015; Ni *et al.*, 2015; Chen *et al.*, 2018).

The wide range of ages (160-130 Ma) obtained on W-Sn deposits from the Nanling Range and the demonstrated involvement of several fluids therefore raise several questions: (i) Can we precisely constrain the age and duration of these events of fluid circulations leading to deposit formation? (ii) Were tungsten and tin deposited at the same time? (iii) Do gangue minerals and associated W-Sn minerals yield the same age? (iv) Did the multiple fluid circulations disturb the isotopic systems of the dated minerals?

The present study focuses on the world-class Maoping W-Sn deposit using a multi-mineral dating approach to unravel the temporal fluid evolution of this magmatic-hydrothermal systems. Here, we combine (i) U-Pb dating of wolframite to constrain the age of W mineralization, (ii) ^{40}Ar - ^{39}Ar dating on several generations of Fe-Li-mica from the syn- to post-mineralization stages, granite, and greisen, and (iii) U-Th-Pb dating of xenotime associated with late-stage REE-minerals postdating the deposition of the W-Sn mineralization. This multi-mineral dating approach is based on a detailed paragenetic sequence and fluid characterization proposed by Legros *et al.* (2016, 2019). The results are compared with those from the literature regarding the Nanling Range to propose a new model for the formation of granite-related W-Sn deposits in Southeast China.

2. Geological setting

2.1 The southern Jiangxi metallogenic province (Nanling Range)

101 The southern Jiangxi metallogenic province is situated within the South China Craton (SCC),
 102 which was assembled during the Neoproterozoic (1000-950 Ma) by the continental collision
 103 between the Yangtze Block in the north and the Cathaysia Block in the south along the
 104 Jiangshan-Shaoxi fault zone (Charvet, 2013; Fig. 1). The SCC was reworked during several
 105 late Neoproterozoic and Middle Paleozoic events (e.g., Wang *et al.*, 2006; Charvet, 2013).
 106 Among these events, basaltic underplating during the Middle Paleozoic Kwansian orogeny
 107 caused dehydration melting in the lower crust at ca. 430-420 Ma resulting in the emplacement
 108 of syn-kinematic S-type granitic bodies that nowadays cover an area of more than 20,000 km²
 109 (e.g., Wang *et al.*, 2011; Xia *et al.*, 2014).

110 The continental collision between the North China Block and South China Block in the late
 111 Triassic resulted in the formation of a new subduction system that triggered the formation of
 112 the largest W-Sn deposits within the southern Jiangxi metallogenic province (Mao *et al.*,
 113 2013; Yuan *et al.*, 2019). The subduction of the Paleo-Pacific oceanic plate beneath the South
 114 China Block lasted from ca. 190 Ma to ca. 90 Ma (Mao *et al.*, 2013) and enhanced the
 115 production of both I- and S-type granitic magmas now covering more than 14,300 km² (Shu *et*
 116 *al.*, 2008 and references therein).

117 Although some skarn and vein-type W-Sn deposits formed during the Late Triassic period
 118 (220-200 Ma) in association with post-collisional granites, around 90% of the W-Sn
 119 mineralization of the southern Jiangxi province is associated with the Jurassic-Cretaceous
 120 magmatism developed under the extensional regime above the subducting plate (Zhou *et al.*,
 121 2006; Li and Li, 2007; Mao *et al.*, 2013; Wang *et al.*, 2016). The granite-related
 122 mineralization emplaced during the Jurassic-Cretaceous times are divided into four periods:
 123 170-160 Ma, 160-150 Ma, 140-130 Ma, and 120-80 Ma, each associated with contrasting
 124 types of mineralization (Zhou *et al.*, 2006; Mao *et al.*, 2013; Zhao *et al.*, 2017). Most of the
 125 W-Sn and rare element deposits were emplaced during the 160-140 Ma and 120-80 Ma

periods, with a metallogenic peak at 160-150 Ma and 100-90 Ma, respectively (Hu and Zhou, 2012; Mao *et al.*, 2013). Tungsten deposits in the southern Jiangxi province include skarn, porphyry, and vein-type mineralization, which dominantly occurs in three parallel granitic belts within the E-W trending Nanling Range.

2.2 The Maoping W-Sn deposit

The world-class Maoping W-Sn deposit is located in the Dayu district of the Southern Jiangxi Province, where numerous W-Sn deposits are currently mined, such as Xihuashan, Piaotang, and Dahutang (Giuliani, 1985; Guo *et al.*, 2012; Mao *et al.*, 2013; Zhang *et al.*, 2017). The Maoping deposit is currently mined underground and hosts resources estimated at 63 kt WO₃ and 32 kt SnO₂ with average grades of 0.93% WO₃ and 0.64% SnO₂ (Feng *et al.*, 2011, Chen *et al.*, 2018).

The Maoping deposit consists of a concealed peraluminous granite (at a depth of ca. 300 m), a greisen orebody at the top of the granitic intrusion, and a dense network of sub-vertical to radial ore-bearing veins rooted in the apical part of the granite and hosted in the surrounding Cambrian quartzites and micaschists (Fig. 2; Feng *et al.*, 2011). The mineralization consists of two types: (i) disseminated wolframite in the greisen body and (ii) wolframite-cassiterite-bearing quartz veins. Most W mineralization is found in more than 400 veins, which range from 5 cm to a few meters in thickness and are up to 400 m long (Feng *et al.*, 2011).

The Tianmenshan granite, outcropping few kilometers away from the mine, was interpreted as a lateral extension of the Maoping granite and was emplaced during the Jurassic at 151.8 ± 2.9 Ma (SHRIMP U-Pb zircon; Feng *et al.*, 2011). The greisen and the veins at Maoping are dated at 155.3 ± 2.8 Ma and 150.2 ± 2.8 Ma, respectively (Re-Os on molybdenite; Feng *et al.*, 2011). The paragenetic succession, based on cross-cutting vein relationships in the mine

galleries and petrographic observations (Figs. 3 and 4), includes four types of veins (I to IV) among seven paragenetic stages (I to VII) (Legros *et al.*, 2016). Four fluid end members have been identified based on mica chemistry and fluid inclusion studies (Legros *et al.*, 2016; 2019).

The first stage (I) consists of centimeter-sized microcline, quartz, and Fe-Li-mica in veins. Legros *et al.* (2016) interpreted these veins to be of magmatic origin. The scarcity and small-size of Fe-Li-mica_{1-I} crystals prevented their isotopic dating. The second stage (II) corresponds to the emplacement of hydrothermal veins filled with centimeter-sized Fe-Li-mica_{2-II} only. The third stage (III) is associated with the formation of the ore-bearing W-Sn veins, which are composed of quartz (Qtz_{2,3-III}), wolframite (Wf_{1-III}), cassiterite (Cst_{1-III}), topaz (Toz_{2-III}), Fe-Li-mica (Fe-Li-mica_{3-III}), molybdenite (Mlb_{1-III}), Fe-Li-muscovite (Fe-Li-ms_{1-III}), and Fe-Mn hydroxides (from the alteration of Fe-Li-mica_{3-III}), crystallizing in that order. Quartz and topaz occur as geodic crystals and usually represent the majority of the vein filling. The cavities are locally filled with euhedral and zoned wolframite and cassiterite crystals. Wolframite and cassiterite are associated with later centimeter-sized Fe-Li-mica_{3-III} at the center of the veins.

The fourth stage (IV) corresponds to the emplacement of banded quartz veins. There are four successive generations of undeformed quartz within these veins (Legros *et al.*, 2016). The banding is underlined by zoned Fe-Li-mica_{4-IV}, among other minerals (topaz, K-feldspar, zircon, columbite-tantalite).

Stages V to VII are present in all four vein types and correspond to the crystallization of fluorite, REE minerals (e.g., xenotime and monazite), as well as sulfides (e.g., sphalerite, chalcopyrite, bismuthinite). Stage VI minerals consist of a succession of fluorite (Fl_{1-VI}), kaolinite (Kln_{1-VI}), and late fluorite (Fl_{2-VI}). The first generation of Fl_{1-VI} is euhedral and free of mineral inclusions, whereas the second (Fl_{2-VI}) generation is anhedral, zoned, and hosts

numerous inclusions of REE-phosphates (i.e., xenotime Xnt_{1-6} and monazite Mnz_{1-6}), REE-fluorides, and REE-carbonates.

3. Analytical methods

Petrographic data were obtained using conventional transmitted and reflected light microscopy and a HITACHI FEG S4800 scanning electron microscope (SEM) equipped with an energy dispersive spectrometer (EDS), using a Si(Li) semi-conductor detector, at the Service Commun de Microscopie Electronique et de Microanalyses (SCMEM) of the GeoRessources laboratory (Vandoeuvre-lès-Nancy, France). Optical cathodoluminescence (CL) imaging was also performed on thin-sections, using a CITL cold cathode instrument CL8200 Mk4 (15 kV and 400 mA).

3.1 Electron microprobe

Electron microprobe analyses (EMPA) of Nb, W, Mn, Fe, and Ta, were performed on wolframite samples and P, Ca, Y, La, Ce, Nd, Sm, Gd, Pr, Dy, Er, Yb on xenotime samples using a CAMECA SX100 instrument equipped with 5 wavelength dispersive spectrometers (WDS) at the GeoRessources laboratory (Vandoeuvre-lès-Nancy, France). Calibration was performed using natural and synthetic oxides and silicates standards (olivine, MnTiO_3 , scheelite, Fe_2O_3 , LiTaO_3 and LiNbO_3 , monazite). A current of 20 nA and an accelerating voltage of 15 kV was used with a counting time of 10 s per element. Total Fe is given as FeO . Results are given in weight per cent oxide (wt.%).

3.2 Laser ablation - inductively coupled plasma - mass spectrometry

Minor and trace element composition of wolframite was measured using a laser ablation - inductively coupled plasma - mass spectrometry (LA-ICP-MS) instrumental setup similar to the one described in Leisen *et al.* (2012) and Lach *et al.* (2013), using a GeoLas excimer laser (ArF, 193 nm, Microlas, Göttingen, Germany) (Günther *et al.*, 1997) coupled to an Agilent 7500c quadrupole ICP-MS at the GeoResources laboratory (Vandoeuvre-lès-Nancy, France). The methodology is identical to the one described in Harlaux *et al.* (2018b) for the analysis of wolframite from the French Massif Central. The laser beam was focused onto the sample surface within a 24.5 cm³ cylindrical ablation cell using a Schwarzschild reflective objective (magnification × 25; numerical aperture 0.4) mounted on an optical microscope (Olympus BX41) equipped with a X–Y motorized stage and a CCD camera. ¹⁸²Tungsten (determined by EMPA) was chosen as internal standard and the NIST SRM 610 (values from Jochum *et al.*, 2011) was used as external standard (accuracy verified with NIST SRM 612) (Longerich *et al.*, 1990), based on the results from Harlaux *et al.* (2018b). The following parameters were used: a fluence of 6 J/cm² and a laser frequency of 5 Hz; He = 0.5 L.min⁻¹ as a carrier gas, mixed with Ar = 1.0 L.min⁻¹ via a cyclone mixer prior to entering the ICP torch. Ablation lines of 60 µm diameter and 200 µm length were performed at a 2 µm/s speed. The following isotopes were measured with a dwell time of 10 ms each: ⁷Li, ²⁴Mg, ⁴⁵Sc, ⁴⁷Ti, ⁵¹V, ⁵⁵Mn, ⁵⁷Fe, ⁵⁹Co, ⁶⁰Ni, ⁶³Cu, ⁶⁶Zn, ⁶⁹Ga, ⁷²Ge, ⁸⁵Rb, ⁸⁸Sr, ⁸⁹Y, ⁹⁰Zr, ⁹³Nb, ⁹⁵Mo, ¹¹¹Cd, ¹¹⁵In, ¹¹⁸Sn, ¹³⁹La, ¹⁴⁰Ce, ¹⁴¹Pr, ¹⁴⁶Nd, ¹⁴⁷Sm, ¹⁵³Eu, ¹⁵⁷Gd, ¹⁵⁹Tb, ¹⁶³Dy, ¹⁶⁵Ho, ¹⁶⁶Er, ¹⁶⁹Tm, ¹⁷²Yb, ¹⁷⁵Lu, ¹⁷⁸Hf, ¹⁸¹Ta, ²⁰⁸Pb, ²⁰⁹Bi, ²³²Th, ²³⁸U. The total time in these conditions was 430 ms per sweep. Data was processed using the Iolite software (Paton *et al.*, 2011).

3.3 ⁴⁰Ar-³⁹Ar dating of Fe-Li-mica

⁴⁰Ar-³⁹Ar analytical work was performed at the University of Manitoba (Canada) using a multi-collector Thermo Fisher Scientific ARGUS VI mass spectrometer, linked to a stainless steel Thermo Fisher Scientific extraction/purification line, Photon Machines (55 W) Fusions 10.6 CO₂ laser, and Photon Machines (Analyte Excite) 193 nm laser. Argon isotopes (from mass 40 to 37) were measured using Faraday detectors with low noise $1 \times 10^{12} \Omega$ resistors and mass 36 was measured using a compact discrete dynode (CDD) detector. All specimens (samples and standard) were irradiated in the Cadmium-lined, in-core CLICIT facility of the TRIGA reactor at the Oregon State University (USA). The duration of irradiation was 17 hours and using Fish Canyon sanidine (Kuiper *et al.*, 2008) and GA1550 biotite (Spell and McDougall, 2003) standards. The samples selected for ⁴⁰Ar-³⁹Ar dating were previously investigated by optical microscopy and SEM, in order to spot homogeneous areas within the analyzed minerals (mica) devoid of alteration, micro-inclusions, or internal zoning. Ablation pits of 100 μm were excavated to an estimated depth of 50 μm . Five argon masses were measured simultaneously over a period of 6 minutes. Measured isotope abundances were corrected for extraction-line blanks, which were determined before every sample analysis. Line blanks in both the Excimer and CO₂ system averaged ~3 fA for mass 40 and ~0.013 fA for mass 36. A value of 295.5 was used for the atmospheric ⁴⁰Ar/³⁶Ar ratio (Steiger and Jäger, 1977) for the purposes of routine measurement of mass spectrometer discrimination using air aliquots, and correction for atmospheric argon in the ⁴⁰Ar-³⁹Ar age calculation. Corrections are made for neutron-induced ⁴⁰Ar from potassium, ³⁹Ar and ³⁶Ar from calcium, and ³⁶Ar from chlorine (Roddick, 1983; Renne *et al.*, 1998; Renne and Norman, 2001). For details see Appendix A.

3.4 U-Pb TIMS dating of wolframite

U-Pb ratios of wolframite were measured at the GFZ German Research Centre for Geosciences (Potsdam, Germany), following the analytical procedure described in detail by Romer and Lüders (2006). Wolframite samples from a mine concentrate and individual centimeter-sized crystals from quartz veins were selected for analyses. Samples were crushed and fragments free of visible alteration, fractures, or overgrowths were selected under the binocular microscope. Surface contamination was removed by washing the samples in warm H₂O and acetone. A ²⁰⁵Pb-²³⁵U tracer was added to the sample and an excess of concentrated HF was used to dissolve the samples on a heated plate overnight (160°C). Precipitation of tungstates before complete sample dissolution may result in incomplete homogenization of tracer and sample, eventually resulting in spuriously old ages. Therefore, all samples were inspected for absence of precipitates.

Pb and U were separated and purified using ion exchange chemistry (Romer *et al.*, 2005) and loaded on separate Re single filaments with H₃PO₄ and colloidal silica. Isotopic ratios of Pb and U were measured on a Triton thermal ionization mass spectrometer (TIMS) using Faraday collectors or an ion counter depending on signal intensity. Data reduction procedures are described in Schmid *et al.* (2003). Concordia diagrams and age calculations were performed using the Isoplot/Ex add-in for Excel (Ludwig, 2008).

3.5 U-Th-Pb LA-ICP-MS dating of xenotime

U-Th-Pb dating of xenotime was performed at the Université de Rennes (Géosciences Rennes, France) using an ESI NWR193UC Excimer laser system and ESI NWR TwoVol2 ablation cell coupled to an Agilent 7700x quadrupole ICP-MS. The laser was operated at a repetition rate of 3 Hz, a fluence of 8 J/cm² and using a spot diameter of 25 µm. The ablated material was transported to the mass spectrometer in He, before mixing with N₂ (Paquette *et*

al., 2014) and Ar, and introduced in the ICP torch equipped with a dual pumping system to enhance sensitivity. Tuning of the instrument and mass calibration were performed before the analytical session using the NIST SRM 612 (Jochum *et al.*, 2011) reference glass, by monitoring the ^{238}U signal and minimizing the ThO^+/Th^+ ratio ($<0.5\%$). The analyses consisted of the acquisition of the $^{204}(\text{Pb} + \text{Hg})$, ^{206}Pb , ^{207}Pb , ^{208}Pb , ^{232}Th and ^{238}U signals. The ^{235}U abundance was calculated from the measured ^{238}U on the basis of a $^{238}\text{U}/^{235}\text{U}$ ratio of 137.818 (Hiess *et al.*, 2012). For each analysis, 20 s of background was integrated, followed by 60 s of laser-generated signal acquisition. Each analysis was separated by a 10 s delay of wash-out. Data reduction was carried out using the GLITTER software package (Van Achterbergh *et al.*, 2001). The Weinsberg xenotime (Klötzli *et al.*, 2007; 317.3 ± 2.0 Ma) standard was used to correct for Pb/U and Pb/Th laser-induced elemental fractionation and instrumental mass discrimination. As we do not have a second xenotime standard, the same standard was analyzed and treated as unknown during the analytical session in order to control the reproducibility and accuracy of the corrections (see results in Supplementary Material A). Twenty analyses yielded a concordia age of 317.5 ± 1.2 Ma (MSWD of $\text{conc} + \text{equiv} = 0.39$). Reproducibility and age uncertainty of our reference material were propagated by quadratic addition to the analyzed xenotime grains according to Horstwood *et al.* (2016). For details of the dating protocol, see Boutin *et al.* (2016). The Concordia plots and age calculations were produced using Isoplot (Ludwig, 2012).

4. Sample descriptions

Thirty-five representative samples of mineralized veins, greisen, and granite were collected at the -5 underground level of the Maoping mine (i.e. approximately 200 m below the current surface). Among the seven paragenetic stages identified at Maoping (Legros *et al.*, 2016; Fig.

4), four of them show a mineralogical diversity allowing a multiple dating approach, namely Stage II Fe-Li-mica veins, Stage III W-Sn veins, Stage IV banded quartz veins, and Stage VI late infillings (Fig. 4). Three types of minerals have been selected for dating: (i) Fe-Li-mica in the granite, the greisen, and three distinct hydrothermal stages; (ii) wolframite to directly date the W mineralization; and (iii) xenotime to determine the formation age of the late fracture-filling stages. U-Pb dating of cassiterite (Stage III and Stage IV) has not been attempted by LA-ICP-MS because of the lack of matrix-matched reference material at the GeoRessources laboratory. Cassiterite is considered to be sub-coeval with wolframite from the Stage III (Legros *et al.*, 2016). The Maoping granite did not contain zircon suitable for U-Pb dating.

4.1 Fe-Li-mica

Representative Fe-Li-mica crystals were sampled from greisen, granite, and all hydrothermal veins (Fig. 5). For detailed mineralogy, major and trace element contents of Fe-Li mica, see Legros *et al.* (2016). All Fe-Li-mica from this study are trioctahedral mica with zinnwaldite composition. Fe-Li-mica_{2-II} was sampled at the selvages of the veins, whereas Fe-Li-mica_{3-III} was taken from the center of the vein. Some crystals show minor alteration with Fe-Li-ms along cleavage planes and local Fe-Mn hydroxides (Fig. 5). Such zones were avoided for *in situ* analyses.

Fe-Li-mica_{4-IV} forms millimeter-sized crystals showing oscillatory zoning (Fig. 5) and having chemical compositions fluctuating between trioctahedral and dioctahedral mica (Legros *et al.*, 2016). Greisen-hosted Fe-Li-mica forms millimeter-sized crystals that resulted from the hydrothermal alteration of the granite (greisenization). Most grains selected for dating show small-scale alteration at the rim and along fractures related to transformation from

trioctahedral to dioctahedral composition. The grains locally contain rare inclusions of hydrothermal fluorite-monazite and uranothorite-monazite assemblages.

Fe-Li-mica from the granite forms small and alteration-free homogeneous crystals (Fig. 5). Rare inclusions of hydrothermal fluorite rimmed by yttrium-carbonate aggregates have been found within the Fe-Li-mica.

4.2 Wolframite

Wolframite typically forms centimeter-sized crystals that are light red under transmitted light, and show micro-porosity, fractures, and evidence of ductile deformation (Legros *et al.*, 2016; 2019). Under the optical microscope, wolframite crystals show fine-scale oscillatory zoning marked by multiple successive growth bands, which do not correlate with changes in major element composition (Fig. 6). Wolframite contains some inclusions of quartz, cassiterite, and sulfides (e.g. bismuthinite). Wolframite generally shows homogeneous major element composition with Mn/(Mn+Fe) varying from 68% to 73%, depending on the degree of hydrothermal alteration (Fig. 6). Wolframite has relatively high concentrations in Nb (1900 to 4100 ppm), Ta (637 to 1100 ppm), HREE (240 to 730 ppm), Sc (135 to 367 ppm), Zn (122 to 178 ppm), Y (59 to 192 ppm), Mo (46 to 157 ppm), Zr (27 to 132 ppm), and Sn (46 to 75 ppm) (LA-ICP-MS; Appendix B). Variations in trace element contents do not correlate with compositional zones within wolframite. Patchy zoning, which is locally observed along minor alteration zones, increases the Mn/Fe ratio of the crystals (Fig. 6). The dated wolframite samples include (i) fragments from a concentrate provided directly from the mine (referred as concentrate thereafter), and (ii) fragments of a single crystal from the Stage III W-Sn vein (referred as vein thereafter).

4.3 Xenotime

Large hydrothermal xenotime grains (50 to 400 μm in size) occur on yttrium-rich growth surfaces of Fl_{2-VI} in association with kaolinite and REE minerals (Legros *et al.*, 2016). Xenotime is anhedral to subhedral and shows no corrosion or dissolution features (Fig. 7). Some grains display textural zoning that cannot be correlated to chemical variations or alteration features (Fig. 7; Appendix C). Xenotime grains have variable amounts of Y₂O₃ (30.0 to 44.0 wt.%), CaO (0.1 to 13.5 wt.%), Dy₂O₃ (4.5 to 9.7 wt.%), Yb₂O₃ (4.0 to 11.4 wt.%), Gd₂O₃ (2.5 to 6.3 wt.%), and Er₂O₃ (3.5 to 5.2 wt.%) as determined by EPMA. These chemical variations do not correlate with the shape of xenotime grains nor their relative position within fluorite. The xenotime grains selected for dating are inclusions within two fluorite samples from a Stage III W-Sn vein, but formed during Stage VI (late filling phases).

5. Results

5.1 ⁴⁰Ar/³⁹Ar Fe-Li-mica dating

The results of all measurements performed on different samples are shown in Table 1 and Figure 8. The ⁴⁰Ar/³⁹Ar apparent ages for Fe-Li-mica_{2-II} range from 167 to 142 Ma and overlap within error. Integration of all data (n=6) yields a date of 157 ± 4 Ma (2 σ , MSWD=1.33; Fig. 8). No compositional variation due to alteration or inclusions correlates with the obtained ages.

The ⁴⁰Ar/³⁹Ar apparent ages for Fe-Li-mica_{3-III} range from 170 to 138 Ma and overlap within error. Excluding the older apparent age of ca. 166.5 Ma, five analyses yield a weighted mean date of 155 ± 4 Ma (2 σ , MSWD = 0.74; Fig. 8).

Fe-Li-mica_{4-IV} from banded quartz veins (Stage IV) is zoned at a too fine scale for in situ analysis of individual growth zones (Fig. 5F). Only the homogeneous external rims of the grains were analyzed. The $^{40}\text{Ar}/^{39}\text{Ar}$ apparent ages range from 167 to 148 Ma. The weighted mean age for five of the six analyses (excluding the younger age of 144.3 Ma because of anomalous Ar ratios) yields a date of 158 ± 4 Ma (2σ , MSWD=1.14; Fig. 8).

Fe-Li-mica from the greisen show alteration along rims and fractures. These zones were carefully avoided during analyses. $^{40}\text{Ar}/^{39}\text{Ar}$ apparent ages range from 167 to 144 Ma. The weighted mean of all six analyses yields a date of 156 ± 2 Ma (2σ , MSWD=1.7; Fig. 8).

Fe-Li-mica from the granite yields $^{40}\text{Ar}/^{39}\text{Ar}$ apparent ages ranging from 166 to 148 Ma. Two analyses yield younger apparent ages of ca. 145 Ma and have been excluded from the age calculation. The remaining seven analyses yield a weighted mean date of 156 ± 2 Ma (2σ , MSWD=0.35; Fig. 8).

5.2 U-Pb wolframite dating

Wolframite has relatively high U contents of 14 to 22 ppm (concentrate) and 8 to 12 ppm (vein sample), whereas Pb contents are below 1.5 ppm with variable contributions of common lead (Table 2). The latter accounts for the large range of measured $^{206}\text{Pb}/^{204}\text{Pb}$ ratios from 55 to 420. The wolframite samples show essentially no variation in $^{208}\text{Pb}/^{204}\text{Pb}$ (37.90 – 39.96), which indicates that the amount of ^{208}Pb coming from the decay of ^{232}Th is insignificant. Sample 9 is an exception (Table 2) since it has a high $^{208}\text{Pb}/^{204}\text{Pb}$ together with a high $^{206}\text{Pb}/^{204}\text{Pb}$. Using $^{208}\text{Pb}_{\text{rad}}/^{206}\text{Pb}_{\text{rad}}$, the measured U contents, and an age of 160 Ma, the Th content for this sample is estimated to be ca. 120 ppm. As Th contents in wolframite are typically low (Romer and Lüders, 2006), this high Th content may indicate that this sample contained micro-inclusions that had high Th contents and slightly higher common Pb contents

than the ambient wolframite. Such inclusion could be monazite explaining this anomalously high Th content. Sample 13 (Table 2) has a high common Pb (29.4 ppm) content, which may be due to small sulfide inclusions. *In situ* growth of radiogenic Pb contributed only insignificantly to the Pb budget of this sample. Therefore, we used the U and Pb concentration and the measured Pb isotopic composition of this sample to estimate the initial Pb isotopic composition of wolframite at 160 Ma. We use this estimate of the initial Pb isotopic composition (Table 2) to calculate the $^{206}\text{Pb}/^{238}\text{U}$ and $^{207}\text{Pb}/^{235}\text{U}$ ratios of the other samples. In the $^{206}\text{Pb}/^{238}\text{U}$ vs. $^{207}\text{Pb}/^{235}\text{U}$ diagram, data for each sample plot in two clusters around 160 and 156 Ma respectively (Figs. 9A and B). Five samples of the concentrate wolframite define a concordant age of 160.4 ± 0.4 Ma (2σ , MSWD (of concordance) = 1.13; Fig. 9C) and three samples of the vein wolframite define a concordant age of 156.3 ± 1.1 Ma (2σ , MSWD (of concordance) = 0.98; Fig. 9D). The two calculated ages are observed both in the concentrate and the vein samples.

5.3 U-Th-Pb xenotime dating

Thirty-four LA-ICP-MS analyses were performed on 27 chemically homogeneous xenotime grains within two fluorite crystals from a single vein (Fig. 10; Table 5; Appendix C). The combined measured U-Th-Pb data are reported in a $^{206}\text{Pb}/^{238}\text{U}$ vs. $^{208}\text{Pb}/^{232}\text{Th}$ concordia diagram (Fig. 10A) rather than in the conventional $^{206}\text{Pb}/^{238}\text{U}$ vs. $^{207}\text{Pb}/^{235}\text{U}$ diagram due to a very low ^{207}Pb signal (average of 650 cps). In the $^{206}\text{Pb}/^{238}\text{U}$ vs. $^{208}\text{Pb}/^{232}\text{Th}$ concordia diagrams, disturbances have the following effect: Pb-loss results in a shift along the concordia. Because of the curvature of the concordia is only small for young samples, Pb-loss will not result in discordance. Uranium and Thorium may be mobilized separately. The loss of U will shift the data spot vertically above the concordia to older apparent $^{206}\text{Pb}/^{238}\text{U}$ ages,

whereas the loss of Th will shift the data spot horizontally below the concordia to older apparent $^{208}\text{Pb}/^{232}\text{Th}$ ages. Samples that do not fall on the concordia have seen such a fractionation of U and Th during alteration (dashed in Fig. 10A), which may go along with Pb mobility. Lead loss, which will spread the data along the concordia, is unlikely to affect all analyzed spots to the same extent. Therefore, the two clusters are interpreted as events. Samples between these two clusters could represent mixtures of the two generations or reflect partial Pb loss.

The samples spread along the Concordia curve with two clusters at the ends of the trend. One cluster with nine concordant analyses yields an age of 152.5 ± 1.3 Ma (2σ , MSWD = 1.9), whereas the other cluster containing nine analyses yields an age of 130.1 ± 1.2 Ma (2σ , MSWD = 2.1; Figs. 10C and D). There is no correlation between the U-Th-Pb age, chemical composition, and relative position of xenotime within the host fluorite crystal.

6. Discussion

Detailed mineralogical studies of the Maoping and other W-Sn deposits in southern China showed that these magmatic-hydrothermal deposits had a multistage fluid evolution, involving the mixing of at least four different fluid types of magmatic or meteoric origin and with contrasting metal endowment (e.g., Tanelli, 1982; Legros *et al.*, 2016, 2018). Isotopic dating of the Maoping deposit indicates a 30 m.y. timespan (160-130 Ma) for the formation of the deposit and subsequent stages of metal redistribution. This interval is in accordance with geochronological data from other W-Sn deposits of southeast China (e.g. Yuan *et al.*, 2007; Liu *et al.*, 2011; Hu *et al.*, 2012a; Zhang *et al.*, 2015; Liu *et al.*, 2017; Deng *et al.*, 2019).

6.1 Four stages of fluid events in the Maoping W-Sn deposit between 160 and 130 Ma

450

451 The ^{40}Ar - ^{39}Ar dating of Fe-Li mica from all samples (granite, greisen, and vein) yield a
452 continuum of (i) overlapping apparent ages ranging from 167 to 142 Ma and (ii) overlapping
453 calculated ages ranging from 158 to 155 Ma. This spread of apparent ages is found for each
454 sample, thus indicating a general trend for micas from Maoping. Moreover, the calculated
455 ages are inconsistent with the crosscutting relations previously described by Legros *et al.*
456 (2016). This would suggest that the ^{40}Ar - ^{39}Ar isotopic system of the Fe-Li mica experienced
457 post-crystallization disturbances. There is no clustering of apparent ages, which may be
458 interpreted in three ways: (i) Fe-Li micas record ages of successive fluid episodes that
459 occurred during a period of 20 m.y., (ii) the obtained dates fall between the time of
460 crystallization and the time of fluid-mediated disturbance of the isotopic systems, or (iii) all
461 samples define a same event at ca. 156 Ma with variable age uncertainties. In the first two
462 cases, the minimum date for the crystallization of Fe-Li-mica would be ca. 167 Ma, whereas
463 the maximum date of the disturbance would be ca. 142 Ma. The third case would be
464 consistent with the second age obtained on the wolframite at 156.3 ± 1.1 Ma.

465 The U-Pb and U-Th-Pb ages on wolframite and xenotime yield respectively two groups of
466 concordant ages. The oldest concordant age at 160.4 ± 0.4 Ma (2σ) is considered to reflect the
467 time of wolframite deposition, whereas the younger age may date the fluid event that
468 perturbed the isotopic systems. This age is consistent within error with the oldest inclusion-
469 free apparent ages for Fe-Li-mica from the veins, granite, and greisen (Fig. 8). This age also
470 correlates with a recent dating study on the coarse-grained Maoping granite giving an age of
471 159.0 ± 1.5 Ma (U-Pb on zircon, Chen *et al.*, 2019). Petrographic observations demonstrate
472 that both mica and wolframite represent early phases in the hydrothermal sequence at
473 Maoping (Legros *et al.*, 2016). The 160 Ma age is consistent with sub-coeval formation of

wolframite-bearing quartz veins subsequently to the intrusion of the Maoping granite. Therefore, the two older ages (ellipses 4 and 5) may represent analytical artifacts. The second age of 156.3 ± 1.1 Ma (2σ) for the Maoping wolframite may correspond to an isotopic reset resulting from local fluid-rock interaction and hydrothermal alteration as indicated by dissolution-replacement textures and a shift toward more Mn-rich chemical compositions (Figs. 6C and D). Such a reset of the U-Pb isotope system of wolframite by alteration has already been described in earlier studies (Harlaux *et al.*, 2018a; Deng *et al.*, 2019). The ca. 156 Ma age is consistent with the scattered Fe-Li-mica ages between ca. 160 Ma and 152 Ma, the Re-Os molybdenite and U-Pb cassiterite ages of 155.3 ± 2.8 Ma and 156.9 ± 1.4 Ma obtained for the greisen (Feng *et al.*, 2011; Chen *et al.*, 2019), and the U-Pb cassiterite age of 156.8 ± 1.5 Ma for the mineralized veins (Chen *et al.*, 2019). Therefore, the ca. 156 Ma age likely represents the circulation of Mo and Sn-rich fluids within the greisen apical body.

The U-Th-Pb isotopic data for xenotime define a trend with two statistically distinguishable clusters corresponding to ages of 152.5 ± 1.3 Ma and 130.1 ± 1.2 Ma respectively (Fig. 11). The age of 152.5 ± 1.3 Ma is identical within error with the Re-Os molybdenite age at 150.2 ± 2.8 Ma for a W-Sn mineralized vein (Feng *et al.*, 2011), and is interpreted as the age of xenotime crystallization. This age does not overlap with the ages obtained on wolframite, indicating that wolframite and xenotime were formed during temporally distinct fluid events at Maoping. The xenotime age of ca. 152 Ma is coeval with the precipitation of a second generation of molybdenite and the main sulfide minerals (Fig. 4), since resetting of the Re-Os isotope system is unlikely (e.g., Stein *et al.*, 2001). This xenotime age correlates with the emplacement of the Tianmenshan intrusion dated at 151.8 ± 5.8 Ma (2σ ; U-Pb SHRIMP on zircon; Feng *et al.*, 2011). The Tianmenshan granite, exposed only few kilometers away from the Maoping mine and which was previously interpreted as a lateral extension of the Maoping

granite (Feng *et al.*, 2011), represents therefore a younger intrusion distinct from the coarse-grained Maoping granite dated at 159.0 ± 1.5 Ma (U-Pb on zircon, Chen *et al.*, 2019). The second calculated age at ca. 130 Ma for xenotime defines the final end-member of a continuum of measured dates starting at ca. 152 Ma. All the intermediate ellipses may reflect variable degrees of disturbance of the U-Th-Pb isotopic system of xenotime, as already described in the literature (e.g. England *et al.*, 2001; Rasmussen *et al.*, 2007; Tartèse *et al.*, 2015; Zi *et al.*, 2015). These variable degrees of disturbance do not correlate with the position of the xenotime grain within the fluorite growth zoning. The ca. 130 Ma age possibly corresponds to the age of the last hydrothermal activity in the Maoping area and may reflect the complete resetting of the isotope system of xenotime. This age is supported by dating of hydrothermal zircon closely associated with xenotime and fluorite from different W-Sn deposits of the Nanling Range (Wang *et al.*, 2016). This would indicate that the remobilizing fluid at 130 Ma was likely to be Zr-REE-rich similarly to the fluid crystallizing the minerals from stage IV and VI at Maoping. This age is also closely associated with the fine-grained granite dated at 125.5 ± 1.3 Ma by U-Pb on zircons (Chen *et al.*, 2019). The geochemistry of this intrusion has not yet been described in detail but it could be the source of this late fluid. The possibility of a second intrusion affecting the Maoping deposit was already suggested by previous studies of Fe-Li-micas geochemistry and fluid inclusions (Legros *et al.*, 2016 and 2019).

Our data define four main age groups (160 Ma – 156 Ma – 152 Ma – 130 Ma) for the W-Sn Maoping deposit, spreading over a period of 30 m.y. This age range is known from other W-Sn deposits in the Nanling Range and is consistent with a scenario of several episodes of fluid flow that resulted both in the addition and redistribution of metals in the Upper Jurassic to Lower Cretaceous.

6.2 Implications for multiple fluid episodes in the W-Sn Dayu district

The Dayu district, located in the southeastern part of the Jiangxi province, is a world-class district for both W and Sn (Fig. 1). Besides the Maoping deposit, eight other W-Sn vein-type deposits have been dated: Zhangdou (Feng *et al.*, 2011), Xihuashan (Hu *et al.*, 2012a), Piaotang (Zhang *et al.*, 2009; Wang *et al.*, 2016; Zhang *et al.*, 2017; Deng *et al.*, 2019), Yaogangxian (Deng *et al.*, 2019), Niuling (Feng *et al.*, 2011), Baxiannao (Feng *et al.*, 2011), Taoxikeng (Wang *et al.*, 2016), and Dangping (Wang *et al.*, 2016). These geochronological studies were focused mainly on mica, molybdenite, zircon, and cassiterite. A compilation of existing data and a comparison with results from the present study reveal that the different deposits have similar ages ranging from ca. 160 to ca. 130 Ma (Fig. 11), with the majority of ages bracketed between 160 Ma and 145 Ma. These findings indicate that the formation of W-Sn deposits and the hydrothermal alteration were controlled by processes that operated on the scale of the entire district.

U-Pb crystallization age of wolframite (159.5 ± 1.3 Ma; Deng *et al.*, 2019) and cassiterite (159.5 ± 1.5 Ma; Zhang *et al.*, 2017) from the Piaotang deposit is contemporaneous within error with the oldest U-Pb age obtained on wolframite for the Maoping deposit (160.4 ± 0.4 Ma, this work). Major W-Sn mineralization in the Dayu district all formed at ca. 160 Ma and were remobilized at ca. 156 Ma. Mica from other W-Sn deposits yielded ^{40}Ar - ^{39}Ar ages of ca. 160 Ma (Fig. 12). Younger ages at ca. 156 Ma, 152 Ma, and 130 Ma (Fig. 11) have been reported from other deposits within the region, indicating that these different ages correspond to regional rather than local events. For instance, fluid circulation episodes at ca. 156 Ma and 152 Ma were reported from deposits within the Dayu district (ca. 50 km wide; Zhang *et al.*, 2009; Feng *et al.*, 2011; Hu *et al.*, 2012a; Deng *et al.*, 2019). Moreover, U-Th-Pb xenotime (this study) and U-Pb age hydrothermal zircon ages (Wang *et al.*, 2016) provide evidence for

a hydrothermal event at ca. 130 Ma. Although these hydrothermal episodes may not be strictly coeval at the regional scale, the similarity of temporal ranges and age clustering for other W-Sn deposits in the Dayu district suggests that the events interpreted at Maoping may be observable at a wider scale in the Nanling Range (Fig. 12).

6.3 Regional considerations: age of W-Sn mineralization episode(s) in the Nanling Range

6.3.1 The ca. 160 Ma W-Sn episode

Fluid inclusion studies of ore-mineral assemblages (wolframite and cassiterite) and gangue minerals (quartz, topaz, and fluorite) have shown that different physico-chemical conditions were recorded. This observation is not restricted to Maoping (Legros *et al.*, 2016, 2018, 2019), but also extends to other W-Sn deposits including Xihuashan (Wei *et al.*, 2012), Yaogangxian (Hu *et al.*, 2012b), Dajishan, Dangping, Piaotang, Pangushan (Ni *et al.*, 2015; Legros *et al.*, 2019), Taoxikeng (Wang *et al.*, 2012), Shimensi (Gong *et al.*, 2015; Wei *et al.*, 2017), Baxiannao (Feng *et al.*, 2012), Shizhuyuan, and Yejiwei (Xuexin *et al.*, 1990). This feature is therefore observed at the regional scale in the southern Jiangxi and Hunan provinces and seems to be a common feature of W-Sn deposits of the Nanling Range. Distinct P-T-X-t conditions recorded in ore and gangue minerals imply that isotopic dating of gangue minerals does not always reflect the age of the mineralization (Legros *et al.*, 2019; this study). Direct U-Pb dating of cassiterite and wolframite (Zhang *et al.*, 2017; Deng *et al.*, 2019; this study) demonstrates that the main episode of W-Sn deposition in the Nanling range occurred at ca. 160 Ma. This age is also obtained for the mica samples. Most mica ^{40}Ar - ^{39}Ar ages, however, are younger than 160 Ma, possibly reflecting (i) mixed ages between different fluid events, (ii) partially or completely reset isotopic ages, or (iii) crystallization ages of gangue minerals

that are not strictly coeval with the ore minerals. Resetting of ^{40}Ar - ^{39}Ar ages or late formation of gangue minerals provides an explanation for the contrasting fluid inclusions in ore and gangue minerals (Legros *et al.*, 2019).

6.3.2 The ca. 130 Ma event: signature of a Cretaceous magmatism?

The metallogenic event at 130 Ma is not well-documented in the Nanling Range. For instance, Wang *et al.* (2016, 2017, and references therein) suggested the existence of a late W-Sn mineralization episode at ca. 130 Ma, based on dating of hydrothermal zircon associated with cassiterite and wolframite and interpreted it to be related to the emplacement of evolved muscovite granites. At Maoping, a late mineral assemblage composed of hydrothermal zircon, REE minerals, and fluorite hosted in banded quartz veins (referred as Nb-Ta-Zr-REE Stage IV and VI in Legros *et al.*, 2016) has been documented. This late hydrothermal overprinting is not related to the W-Sn mineralization, but corresponds to a late Nb-Ta-Zr-Y-HREE mineralization, which could be related to peralkaline rare-metal magmatism (e.g., Černý *et al.*, 2005; Linnen and Cuney, 2005). Consequently, this geochemical signature may be interpreted as the chemical footprint of magmatic-hydrothermal fluids exsolved from an unexposed magmatic body at depth (Legros *et al.*, 2016, 2018), similarly to what described in the Puy-les-Vignes W deposit in the French Massif Central (Harlaux *et al.*, 2015a, 2015b, 2019). This intrusion might be the fine-grained granite recently dated at 125.5 ± 1.3 Ma (U-Pb on zircon; Chen *et al.*, (2019)).

7. Conclusion

New geochronological data on the world-class Maoping W-Sn deposit coupled to data from the literature demonstrates that multiple episodes of fluid circulation affected the world class W-Sn Nanling Range province during the Upper Jurassic to Lower Cretaceous (ca. 160 to 130 Ma). We propose the existence of four successive hydrothermal stages: (i) W-Sn bearing fluids at ca. 160 Ma related to the formation of the economic wolframite mineralization, (ii) Mo and Sn-rich fluids at ca. 156 Ma induced alteration of wolframite and resetting of its U-Pb system, (iii) REE-bearing mineralizing fluids precipitated xenotime and sulfides as cavity-filling at ca. 152 Ma, and (iv) REE- and Zr-rich fluids circulating at ca. 130 Ma, possibly related to unexposed magmatic intrusions. We conclude that deposition of wolframite at ca. 160 Ma was followed by several episodes of hydrothermal activity that disturbed the ^{40}Ar - ^{39}Ar , U-Pb and U-Th-Pb isotopic systems of Fe-Li-mica, wolframite, and xenotime. Based on previous petrographic and fluid inclusion studies on the Maoping deposit (Legros et al., 2016, 2018, 2019), our results demonstrate that multiple episodes of fluid circulations may result in partial to complete isotopic resetting of minerals and that gangue minerals do not necessarily date the age of W-Sn mineralization. Isotopic dating of paragenetically well-constrained minerals is critical for determining the age and the duration of mineralizing processes and for characterizing the fluid evolution of magmatic-hydrothermal systems, as exemplified in the Nanling Range.

Acknowledgements

This research was supported by the collaboration between Carnot ICEEL-Nancy and Carnot BRGM-Orléans. Access to the Maoping and Piaotang deposit, and underground sampling was gratefully appreciated, particularly the assistance provided by Zeying Zhu, Xudong Che, Guanglai Li and local miners. RCW's research is supported by the NSF of China (Grant no.

623 41230315), and the MOE-SAFE Affairs of China joint “111” programme (Grant no. B13021).
624 The authors thank A. Lecomte and O. Rouer from the SCMEM (GeoRessources, Nancy) for
625 SEM and EPMA analyses. Finally, we would like to thank the Editor Huayong Chen and two
626 anonymous reviewers for their comments that helped improving the manuscript.
627

References

- Bai, X.J., Wang, M., Lu, K.H., Fang, J.L., Pu, Z.P., Qiu, H.N., 2011. Direct dating of cassiterite by $^{40}\text{Ar}/^{39}\text{Ar}$ progressive crushing. *Chinese Science Bulletin* 56, 1899–1904 (in Chinese).
- Bai, X.J., Wang, M., Jiang, Y.D., Qiu, H.N., 2013. Direct dating of tin-tungsten mineralization of the Piaotang tungsten deposit, South China, by $^{40}\text{Ar}/^{39}\text{Ar}$ progressive crushing. *Geochimica et Cosmochimica Acta* 114, 1–12.
- Best, M.G., Christiansen, E.H., Deino, A.L., Grommé, C.S., Tingey, D.G., 1995. Correlation and emplacement of a large, zoned, discontinuously exposed ash flow sheet; the $^{40}\text{Ar}/^{39}\text{Ar}$ chronology, paleomagnetism, and petrology of the Pahrnagat Formation, Nevada. *Journal of Geophysical Research* 100, 24593–24609.
- Boutin, A., de Saint Blanquat, M., Poujol, M., Boulvais, P., de Parseval, P., Rouleau, C., Robert, J.-F., 2016. Succession of Permian and Mesozoic metasomatic events in the eastern Pyrenees with emphasis on the Trimouns talc-chlorite deposit. *International Journal of Earth Sciences* 105, 747–770.
- Černý, P., Blevin, P.L., Cuney, M., London, D., 2005. Granite-related ore deposits. *Society of Economic Geologists* 100, 337–370.
- Charvet, J., 2013. The Neoproterozoic-Early Paleozoic tectonic evolution of the South China Block: an overview. *Journal of Asian Earth Sciences* 74, 198–209.
- Chen, Z.H., Chen, Y.C., Wang, D.H., 2009. Demonstration studies for assessment of mineral resources potential: Case study of the potential assessment of tungsten resources in East Nanling Range. Geological Publishing House, Beijing, 1–195 (in Chinese).
- Chen, L.L., Ni, P., Li, W.S., Ding, J.Y., Pan, J.Y., Wang, G.G., Yang, Y.L., 2018. The link between fluid evolution and vertical zonation at the Maoping tungsten deposit, Southern

653 Jiangxi, China: Fluid inclusion and stable isotope evidence. *Journal of Geochemical*
654 *Exploration* 192, 18–32.

655 Chen, L. L., Ni, P., Dai, B. Z., Li, W. S., Chi, Z., Pan, J. Y., 2019. The Genetic Association
656 between Quartz Vein-and Greisen-Type Mineralization at the Maoping W–Sn Deposit,
657 Southern Jiangxi, China: Insights from Zircon and Cassiterite U–Pb Ages and
658 Cassiterite Trace Element Composition. *Minerals* 9, 411.

659 Dazé, A., Lee, J.K., Villeneuve, M., 2003. An intercalibration study of the Fish Canyon
660 sanidine and biotite $^{40}\text{Ar}/^{39}\text{Ar}$ standards and some comments on the age of the Fish
661 Canyon Tuff. *Chemical Geology* 199, 111–127.

662 Deng, X.-D., Luo, T., Li, J.-W., Hu, Z.-C., 2019. Direct dating of hydrothermal tungsten
663 mineralization using in situ wolframite U–Pb chronology by laser ablation ICP-MS.
664 *Chemical Geology*, <https://doi.org/10.1016/j.chemgeo.2019.04.005> (in press).

665 England, G.L., Rasmussen, B., McNaughton, N.J., Fletcher, I.R., Groves, D.I., Krapez, B.,
666 2001. SHRIMP U–Pb ages of diagenetic and hydrothermal xenotime from the Archaean
667 Witwatersrand Supergroup of South Africa. *Terra Nova* 13, 360–367.

668 Feng, C., Zeng, Z., Zhang, D., Qu, W., Du, A., Li, D., She, H., 2011. SHRIMP zircon U–Pb
669 and molybdenite Re–Os isotopic dating of the tungsten deposits in the Tianmenshan–
670 Hongtaoling W–Sn orefield, southern Jiangxi Province, China, and geological
671 implications. *Ore Geology Reviews* 43, 8–25.

672 Feng, C.Y., Wang, S., Zeng, Z.L., Zhang, D.H., Li, D.X., She, H.Q., 2012. Fluid inclusion
673 and chronology studies of Baxiannao mineralized fractured zone-type tungsten
674 polymetallic deposit, southern Jiangxi Province, China. *Acta Petrologica Sinica* 28, 52–
675 64 (in Chinese with English abstract).

676 Feng, C., Zhao, Z., Qu, W., Zeng, Z., 2015. Temporal consistency between granite evolution
677 and tungsten mineralization in the Huamei'ao, southern Jiangxi Province, China:

678 Evidence from precise zircon U-Pb, molybdenite Re-Os, and muscovite ^{40}Ar - ^{39}Ar
679 isotope geochronology. *Ore Geology Reviews* 65, 1005–1020.

680 Fu, J., Li, H., Qu, W., Yang, X., Wei, J., Liu, G., Ma, L., 2007. Re-Os isotope dating for the
681 Daao tungsten-tin deposit in Jiuyishan area, southern Hunan province. *Geology in*
682 *China* 34, 651–656 (in Chinese with English abstract).

683 Fu, J., Li, H., Qu, W., Ma, L., Yang, X., Wei, J., Liu, G., 2008. Determination mineralization
684 epoch of quartz-vein type tungsten deposits in shixing region, northern Guangdong and
685 its geological significance. *Geotectonica et metallogenia* 32, 57–62 (in Chinese with
686 English abstract).

687 Giuliani, G., 1985. Le gisement de tungstène de Xihuashan (Sud-Jiangxi, Chine): Relations
688 granites, alterations deutériques-hydrothermales, minéralisations. *Mineralium Deposita*
689 20, 107–115.

690 Gong, X.D., Yan, G.S., Ye, T.Z., Zhu, X.Y., Li, Y.S., Zhang, Z.H., Jia, W.B., Yao, X.F.,
691 2015. A study of ore-forming fluids in the Shimensi Tungsten Deposit, Dahutang
692 Tungsten Polymetallic Ore Field, Jiangxi Province, China. *Acta Geologica Sinica* 89,
693 822–835.

694 Günther, D., Frischknecht, R., Heinrich, C.A., Kahlert, H.J., 1997. Capabilities of an argon
695 fluoride 193 nm excimer laser for laser ablation inductively coupled plasma mass
696 spectrometry microanalysis of geological materials. *Journal of Analytical Atomic*
697 *Spectrometry* 12, 939–944.

698 Guo, C., Mao, J., Bierlein, F., Chen, Z., Chen, Y., Li, C., Zeng, Z., 2011. SHRIMP U-Pb
699 (zircon), Ar-Ar (muscovite) and Re-Os (molybdenite) isotopic dating of the Taoxikeng
700 tungsten deposit, South China Block. *Ore Geology Reviews* 43, 26–39.

701 Guo, F., Fan, W.M., Li, C.W., Zhao, L., Li, H.X., Yang, J.H., 2012. Multi-stage crust-mantle
702 interaction in SE China: temporal, thermal and compositional constraints from the
703 Mesozoic felsic rocks in eastern Guangdong-Fujian provinces. *Lithos* 150, 62–84.

704 Harlaux, M., Marignac, C., Cuney, M., Mercadier, J., 2015a. The Puy-les-Vignes breccia pipe
705 (Massif Central, France): a unique occurrence of polymetallic W-Nb±Ta-HREE-Bi-Cu-
706 As±Au-Ag mineralization in the Variscan belt. In: 13th Biennial SGA Meeting Nancy 2,
707 749–752.

708 Harlaux, M., Marignac, C., Cuney, M., Mercadier, J., Magott, R., Mouthier, B., 2015b. Nb-
709 Ti-Y-HREE-W-U oxide minerals with uncommon compositions associated with the
710 tungsten mineralization in the Puy-les-Vignes deposit (Massif Central, France):
711 evidence for rare-metal mobilization by late hydrothermal fluids with a peralkaline
712 signature. *Canadian Mineralogist* 53, 653–672.

713 Harlaux, M., Romer, R.L., Mercadier, J., Morlot, C., Marignac, C., Cuney, M., 2018a. 40 Ma
714 of hydrothermal W mineralization during the Variscan orogenic evolution of the French
715 Massif Central revealed by U-Pb dating of wolframite. *Mineralium Deposita* 53, 21–51.

716 Harlaux, M., Mercadier, J., Marignac, C., Peiffert, C., Cloquet, C., Cuney, M., 2018b. Tracing
717 metal sources in peribatholithic hydrothermal W deposits based on the chemical
718 composition of wolframite: The example of the Variscan French Massif Central.
719 *Chemical Geology* 479, 58-85.

720 Harlaux, M., Mercadier, J., Marignac, C., Villeneuve, J., Mouthier, B., Cuney, M., 2019.
721 Origin of the atypical Puy-les-Vignes W breccia pipe (Massif Central, France)
722 constrained by trace element and boron isotopic composition of tourmaline. *Ore*
723 *Geology Reviews* 114, 103-132.

724 Hiess, J., Condon, DJ, McLean, N, Noble, SR, 2012. $^{238}\text{U}/^{235}\text{U}$ systematics in terrestrial
725 uranium-bearing minerals. *Science* 335:1610-1614

726 Horstwood, M.S., Košler, J., Gehrels, G., Jackson, S. E., McLean, N. M., Paton, C., Pearson,
 727 N.J., Sircombe, K., Sylvester, P., Vermeesch, P., Bowring, J.F., Condon, D.J, Schoene,
 728 B., (2016). Community-derived standards for LA-ICP-MS U-(Th-) Pb geochronology–
 729 Uncertainty propagation, age interpretation and data reporting. *Geostandards and*
 730 *Geoanalytical Research* 40, 311-332.

731 Hu, R.Z., Zhou, M.F., 2012. Multiple Mesozoic mineralization events in South China—an
 732 introduction to the thematic issue. *Mineralium Deposita* 47, 579–588.

733 Hu, R.Z., Wei, W.F., Bi, X.W., Peng, J.T., Qi, Y.Q., Wu, L.Y., Chen, Y.W., 2012a.
 734 Molybdenite Re–Os and muscovite $^{40}\text{Ar}/^{39}\text{Ar}$ dating of the Xihuashan tungsten deposit,
 735 central Nanling district, South China. *Lithos* 150, 111–118.

736 Hu, R.Z., Bi, X.W., Jiang, G.H., Chen, H.W., Peng, J.T., Qi, Y.Q., Wu, L.Y., Wei, W.F.,
 737 2012b. Mantle-derived noble gases in ore-forming fluids of the granite-related
 738 Yaogangxian tungsten deposit, Southeastern China. *Mineralium Deposita* 47, 623–632.

739 Huang, F., Feng, C., Chen, Y., Ying, L., Chen, Z., Zeng, Z., Qu, W., 2011. Isotopic
 740 chronological study on Huangsha-Tieshalong quartz vein type tungstan deposit and
 741 timescale of molybdenum mineralization in southern Jiangxi Province, China. *Acta*
 742 *Geologica Sinica (English edition)* 85, 1434–1447.

743 Huang, F., Wang, D., Santosh, M., Wang, C., Zeng, Z., Liu, S., Wang, L., Zhang, Y., 2014.
 744 Genesis of the Yuanlingzhai porphyry molybdenum deposit, Jiangxi province, South
 745 China: Constraints from petrochemistry and geochronology. *Journal of Asian Earth*
 746 *Sciences* 79, 759–776.

747 Jackson, S.E., Pearson, N.J., Griffin, W.L., Belousova, E.A., 2004. The application of laser
 748 ablation-inductively coupled plasma-mass spectrometry to in situ U-Pb zircon
 749 geochronology. *Chemical Geology* 211, 47–69.

750 Jiang, Y-H., Jiang, S.Y., Zhao, K.D., Ling, H.F., 2006. Petrogenesis of Late Jurassic
751 Qianlishan granites and mafic dykes, southeast China; implications for a back-arc
752 extension setting. *Geology Magazine* 143, 457–474.

753 Jiang, H., Jiang, S.Y., Li, W. Q., Zhao, K.D., Peng, N.J., 2018. Highly fractionated Jurassic I-
754 type granites and related tungsten mineralization in the Shirenzhang deposit, northern
755 Guangdong, South China: Evidence from cassiterite and zircon U-Pb ages,
756 geochemistry and Sr-Nd-Pb-Hf isotopes. *Lithos* 312, 186–203.

757 Jochum, K.P., Weis, U., Stoll, B., Kuzmin, D., Yang, Q., Raczek, I., Jacob, D.E., Stracke, A.,
758 Birbaum, K., Frick, D.A., Gunther, D., Enzweiler, J., 2011. Determination of reference
759 values for NIST SRM 610-617 glasses following ISO guidelines. *Geostandards and*
760 *Geoanalytical Research* 35, 397–429.

761 Klötzli, E., Klötzli, U., Kosler, J., 2007. A possible laser ablation xenotime U-Pb age
762 standard: reproducibility and accuracy. *Geochimica et Cosmochimica Acta* 71, A495.

763 Kuiper, K.F., Deino, A., Hilgen, F.J., Krijgsman, W., Renne, R., Wijbrans, J.R., 2008.
764 Synchronizing Rock Clocks of Earth History. *Science* 320, 500–504.

765 Lach, P., Mercadier, J., Dubessy, J., Boiron, M.C., Cuney, M., 2013. In situ quantitative
766 measurement of rare earth elements in uranium oxides by laser ablation-inductively
767 coupled plasma-mass spectrometry. *Geostandards and Geoanalytical Results* 37, 1–20.

768 Lecumberri-Sanchez, P., Romer, R.L., Luders, V., Bodnar, R.J., 2014. Genetic relationship
769 between silver-lead-zinc mineralization in the Wutong deposit, Guangxi Province and
770 Mesozoic granitic magmatism in the Nanling belt, southeast China. *Mineralium*
771 *Deposita* 49, 353–396.

772 Leisen, M., Boiron, M.C., Richard, A., Dubessy, J., 2012. Determination of Cl and Br
773 concentrations in individual fluid inclusions by combining microthermometry and LA-

774 ICPMS analysis: Implications for the origin of salinity in crustal fluids. *Chemical*
775 *Geology* 330–331, 197–206.

776 Legros, H., Marignac, C., Mercadier, J., Cuney, M., Richard, A., Wang, R-C., Charles, N.,
777 Lespinasse, M-Y., 2016. Detailed paragenesis and Li-mica compositions as recorders of
778 the magmatic-hydrothermal evolution of the Maoping W-Sn deposit (Jiangxi, China).
779 *Lithos* 264, 108–124.

780 Legros, H., Marignac, C., Tabary, T., Mercadier, J., Richard, A., Cuney, M., Wang, R-C.,
781 Charles, N., Lespinasse, M-Y., 2018. The ore-forming magmatic-hydrothermal system
782 of the Piaotang W-Sn deposit (Jiangxi, China) as seen from Li-mica geochemistry.
783 *American Mineralogist* 103, 39–54.

784 Legros, H., Richard, A., Tarantola, A., Kouzmanov, K., Mercadier, J., Vennemann, T.,
785 Marignac, C., Cuney, M., Wang, R-C., Charles, N., Bailly, L., Lespinasse, M-Y., 2019.
786 Multiple fluids involved in granite-related W-Sn deposits from the world-class Jiangxi
787 Province (China). *Chemical Geology* 508C, 92–115.

788 Li, Z. X., and Li, X. H., 2007. Formation of the 1300-km-wide intracontinental orogen and
789 postorogenic magmatic province in Mesozoic South China: a flat-slab subduction
790 model. *Geology* 35, 179-182.

791 Li, X., Xiao, R., Feng, Z., 2011. Major types and metallogenic epoch of metallic deposits in
792 northeastern Guangxi, and its geological significances. *Acta Mineralogica Sinica* 31,
793 610–611 (in Chinese).

794 Li, L.X., Chen, Z.H., Shi, G.H., Zhang, S.M., Qu, W.J., Ying, L.J., Qin, Y., Ding, Q., 2014.
795 Metallogenic epoch and geological characteristics of the Kuimeishan tungsten deposit,
796 Jiangxi Province. *Rock and Mineral Analysis* 33, 287–295 (in Chinese with English
797 abstract).

798 Liang, X., Dong, C., Jiang, Y., Wu, S., Zhou, Y., Zhu, H., Fu, J., Wang, C., Shan, Y., 2016.
799 Zircon U-Pb, molybdenite Re-Os and muscovite Ar-Ar isotopic dating of the Xitian W-
800 Sn polymetallic deposit, eastern Hunan Province, South China and its geological
801 significance. *Ore Geology Reviews* 78, 85–100.

802 Linnen, R.L., Cuney, M., 2005. Granite-related rare-element deposits and experimental
803 constraints on Ta-Nb-W-Sn-Zr-Hf mineralization. In: Linnen, R.L., Samson, I.M.
804 (Eds.), *Rare-element geochemistry and mineral deposits*. Geological Association of
805 Canada, GAC Short Course Notes 17, 45–68.

806 Liu, S., Wang, D.H., Chen, Y., Li, J., Ying, L., Xu, J., Zeng, Z., 2008. $^{40}\text{Ar}/^{39}\text{Ar}$ ages of
807 muscovite from the different types tungsten-bearing quartz veins in the Chong-Yu-You
808 concentrated mineral area in gannan region and its geological significance. *Acta*
809 *Geologica Sinica* 82, 932–940. (in Chinese with English abstract)

810 Liu, S., Chen, Y., Fan, S., Xu, J., Qu, W., Ying, L., 2010. The second ore-prospecting space
811 in the eastern and central parts of the Nanling metallogenic belt: evidence from isotopic
812 chronology. *Geology in China* 37, 1034–1049. (in Chinese with English abstract)

813 Liu, J., Mao, J., Ye, H., Zhang, W., 2011. Geology, geochemistry and age of the Hukeng
814 tungsten deposit, Southern China. *Ore Geology Reviews* 43, 50–61.

815 Liu, P., Mao, J., Cheng, Y., Yao, W., Wang, X., Hao, D., 2017. An early cretaceous W-Sn
816 deposit and its implications in southeast coastal metallogenic belt: Constraints from U-
817 Pb, Re-Os, Ar-Ar geochronology at the Feie'shan W-Sn deposit, SE China. *Ore*
818 *Geology Reviews* 81, 112–122.

819 Longerich, H.P., Jenner, G.A., Fryer, B.J., Jackson, S.E., 1990. Inductively coupled plasma-
820 mass spectrometric analysis of geological samples: a critical evaluation based on case
821 studies. *Chemical Geology* 83, 105–118.

822 Ludwig, K.R., 2008. Isoplot/Ex Version 3.70: A Geochronological Toolkit for Microsoft
 823 Excel. Berkeley Geochronology Center, Spec Pub 4, 73 pp.

824 Ludwig, K.R., 2012. User's Manual for Isoplot 3.75. A geochronological toolkit for Microsoft
 825 Excel. Berkeley Geochronological Center, 1–75.

826 Mao, J., Xie, G., Li, X., Zhang, C., Wang, Y., 2006. Mesozoic large-scale mineralization and
 827 multiple lithospheric extensions in South China. *Acta Geologica Sinica* 80, 420–431.

828 Mao, J., Pirajno, F., Cook, N., 2011. Mesozoic metallogeny in East China and corresponding
 829 geodynamic settings — an introduction to the special issue. *Ore Geology Reviews* 43,
 830 1–7.

831 Mao, Z., Cheng, Y., Liu, J., Yuan, S., Wu, S., Xiang, X., Luo, X., 2013. Geology and
 832 molybdenite Re-Os age of the Dahutang granite-related veinlets-disseminated tungsten
 833 ore field in the Jiangxi Province, China. *Ore Geology Reviews* 53, 422–433.

834 Ni, P., Wang, X.D., Wang, G.G., Huang, J.B., Pan, J.Y., Wang, T.G., 2015. An infrared
 835 microthermometric study of fluid inclusions in coexisting quartz and wolframite from
 836 Late Mesozoic tungsten deposits in the Gannan metallogenic belt, South China. *Ore
 837 Geological Reviews* 65, 1062–1077.

838 Paquette, J.L., Piro, J.L., Devidal, J.L., Bosse, V., Didier, A., Sanac, S., Abdelnour, Y., 2014.
 839 Sensitivity enhancement in LA-ICP-MS by N₂ addition to carrier gas: Application to
 840 radiometric dating of U-Th-bearing minerals. *Agilent ICP-MS Journal* 58, 1–5.

841 Paton, C., Hellstrom, J., Paul, B., Woodhead, J., Hergt, J., 2011. Iolite: Freeware for the
 842 visualization and processing of mass spectrometric data. *Journal of Analytical Atomic
 843 Spectrometry* 26, 2508–2518.

844 Peng, J.T., Zhou, M.F., Hu, R.Z., Shen, N.P., Yuan, S.D., Bi, X.W., Du, A.D., Qu, W.J.,
 845 2006. Precise molybdenite Re-Os and mica Ar-Ar dating of the mesozoic Yaogangxian

846 tungsten deposit, central Nanling district, South China. *Mineralium Deposita* 41, 661–
847 670.

848 Qi, H-W., Hu, R-Z., Wang, X-F., Qu, W-J., Bi, X-W., Peng, J-T., 2012. Molybdenite Re-Os
849 and muscovite $^{40}\text{Ar}/^{39}\text{Ar}$ dating of quartz vein-type W-Sn polymetallic deposits in
850 Northern Guangdong, South China. *Mineralium Deposita* 47, 607–622.

851 Rasmussen, B., Fletcher, I.R., Muhling, J.R., Thorne, W.S., Broadbent, G.C., 2007. Prolonged
852 history of episodic fluid flow in giant hematite ore bodies: evidence from in situ U–Pb
853 geochronology of hydrothermal xenotime. *Earth and Planetary Science Letters* 258,
854 249–259.

855 Renne, P.R., Norman, E.B., 2001. Determination of the half-life of ^{37}Ar by mass
856 spectrometry. *Physical Review C* 63, 047302.

857 Renne, P.R., Swisher, C.C., Deino, A.L., Karner, D.B., Owens, T.L., DePaolo, D.J., 1998.
858 Intercalibration of standards, absolute ages and uncertainties in $^{40}\text{Ar}/^{39}\text{Ar}$ dating.
859 *Chemical Geology* 145, 117–152.

860 Renne, P.R., Cassata, W.S., Morgan, L.E., 2009. The isotopic composition of atmospheric
861 argon and $^{40}\text{Ar}/^{39}\text{Ar}$ geochronology: time for a change? *Quaternary Geochronology* 4,
862 288–298.

863 Roddick, J.C., 1983. High precision intercalibration of ^{40}Ar - ^{39}Ar standards. *Geochimica et*
864 *Cosmochimica Acta* 47, 887–898.

865 Romer, R.L., Lüders, V., 2006. Direct dating of hydrothermal W mineralization: U-Pb age for
866 hübnerite (MnWO_4), Sweet Home Mine, Colorado. *Geochimica et Cosmochimica Acta*
867 70, 4725–4733.

868 Romer, R.L., Kroner, U., 2016. Phanerozoic tin and tungsten mineralization—tectonic
869 controls on the distribution of enriched protoliths and heat sources for crustal melting.
870 *Gondwana Research* 31, 60–95.

871 Romer, R.L., Heinrich, W., Schröder-Smeibidl, B., Meixner, A., Fischer, C.O., Schulz, C.,
 872 2005. Elemental dispersion and stable isotope fractionation during reactive fluid-flow
 873 and fluid immiscibility in the Bufa del Diente aureole, NE-Mexico: Evidence from
 874 radiographies and Li, B, Sr, Nd, and Pb isotope systematics. *Contributions to*
 875 *Mineralogy and Petrology* 149, 400–429.

876 Schmid, R., Romer, R.L., Franz, L., Oberhänsli, R., Martinotti, G., 2003. Basement-cover
 877 sequences within the UHP unit of the Dabie Shan. *Journal of Metamorphic Geology* 21,
 878 531–538.

879 Shu, L., Faure, M., Wang, B., Zhou, X., Song, B., 2008. Late Palaeozoic–Early Mesozoic
 880 geological features of South China: response to the Indosinian collision events in
 881 Southeast Asia. *Comptes Rendus Geoscience* 340, 151–165.

882 Spell, T.L., McDougall, I., 2003. Characterization and calibration of $^{40}\text{Ar}/^{39}\text{Ar}$ dating
 883 standards. *Chemical Geology* 198, 189–211.

884 Steiger, R.H., Jäger, E., 1977. Subcommittee on geochronology: convention on the use of
 885 decay constants in geo- and cosmochemistry. *Earth and Planetary Science Letters* 36,
 886 359–362.

887 Stein, H.J., Markey, R.J., Morgan, J.W., Hannah, J.L., Scherstén, A., 2001. The remarkable
 888 Re–Os chronometer in molybdenite: how and why it works. *Terra Nova* 13, 479–486.

889 Sun, W.D., Yang, X.Y., Fan, W.M., Wu, F.Y., 2012. Mesozoic large scale magmatism and
 890 mineralization in South China: preface. *Lithos* 150, 1–5.

891 Tanelli, G., 1982. Geological setting, mineralogy and genesis of tungsten mineralization in
 892 Dayu district, Jiangxi (People's Republic of China): an outline. *Mineralium Deposita* 17,
 893 279–294.

894 Tartèse, R., Poujol, M., Gloaguen, E., Boulvais, P., Drost, K., Košler, J., Ntaflos, T., 2015.
 895 Hydrothermal activity during tectonic building of the Variscan orogen recorded by U-

896 Pb systematics of xenotime in the Grès Armorica formation, Massif Armorica, France. *Mineralogy and Petrology* 109, 485–500.

897

898 Van Achterbergh, E., Ryan, C.G., Jackson, S.E., Griffin, W., 2001. Data reduction software for LA-ICP-MS. In: Sylvester, P. (Ed.), *Laser Ablation-ICPMS in the Earth Sciences*. Mineralogical Association of Canada Short Course 29, 239–243.

899

900

901 Wang, Y., Fan, B., 1987. In: Guo, W. (Eds.), *Metallogenic map of endogenic ore deposits of China 1:4000000*. Cartographic, Beijing.

902

903 Wang, Z.Q., Yin, C.Y., Gao, L.Z., Tang, F., Liu, Y.Q., Liu, P.J., 2006. The character of the chemical index of alteration and discussion of subdivision and correlation of the Nanhua System in Yichang area. *Geological Review* 52, 577–585.

904

905

906 Wang, D.H., Chen, Z.H., Chen, Y.C., Tang, J.X., Li, J.K., Ying, L.J., Wang, C.J., Liu, S.B., Li, L.X., Qin, Y., Li, H.Q., Qu, W.J., Wang, Y.B., Chen, W., Zhang, Y., 2010a. New data of the rock-forming and ore-forming chronology for China's important resources areas. *Acta Geologica Sinica* 84, 1030–1040. (in Chinese with English Abstract)

907

908

909

910 Wang, X., Qi, H., Hu, R., Qu, W., Peng, J., Bi, X., 2010b. Re-Os isotopic chronology of molybdenites from Hongling tungsten deposit of Guangdong province and its geological significance. *Mineral Deposits* 29, 415–426. (in Chinese with English abstract)

911

912

913

914 Wang, Y., Zhang, A., Fan, W., Zhao, G., Zhang, G., Zhang, Y., Li, S., 2011. Kwangsian crustal anatexis within the eastern South China Block: geochemical, zircon U–Pb geochronological and Hf isotopic fingerprints from the gneissoid granites of Wugong and Wuyi–Yunkai Domains. *Lithos* 127, 239–260.

915

916

917

918 Wang, Q.Y., Lu, Y.F., Chen, Z.H., Peng, X.L., Xiong, X.F., 2012. Fluid inclusion characteristic and its geological implication of the Taoxikeng tungsten deposit, southern Jiangxi Province. *Geology and Mineral Resources of South China* 1(006).

919

920

921 Wang, X., Chen, J., Ren, M., 2016. Hydrothermal zircon geochronology: Age constraint on
 922 Nanling Range tungsten mineralization (Southeast China). *Ore Geology Reviews* 74,
 923 63–75.

924 Wang, X., Ren, M., Chen, J., 2017. The muscovite granites: Parental rocks to the Nanling
 925 Range tungsten mineralization in South China. *Ore Geology Reviews* 88, 702–717.

926 Wei, W., Hu, R., Bi, X., Peng, J., Su, W., Song, S., Shi, S., 2012. Infrared microthermometric
 927 and stable isotopic study of fluid inclusions in wolframite at the Xihuashan tungsten
 928 deposit, Jiangxi province, China. *Mineralium Deposita* 47, 589–605.

929 Wei, W.F., Yan, B., Shen, N.P., Liu, L., Zhang, Y., Xiang, X.K., 2017. Muscovite $^{40}\text{Ar}/^{39}\text{Ar}$
 930 age and H-O-S isotopes of the Shimensi tungsten deposit (Northern Jiangxi Province,
 931 South China) and their metallogenic implications. *Minerals* 7, 162, 15 pp.

932 Wu, C.Y., Bai, G., Xu, L.M., 1993. Types and distribution of silver ore deposits in China.
 933 *Mineralium Deposita* 28, 223–238.

934 Xi, B., Zhang, D., Zhou, L., Zhang, W., Wang, C., 2008. Characteristics of ore forming fluid
 935 evolution in Dajishan Tungsten Deposit, Quannan County, Jiangxi. *Acta Geologica*
 936 *Sinica* 82, 956–966.

937 Xia, Y., Xu, X.S., Zou, H.B., Liu, L., 2014. Early Paleozoic crust-mantle interaction and
 938 lithosphere delamination in South China Block: evidence from geochronology,
 939 geochemistry, and Sr-Nd-Hf isotopes of granites. *Lithos* 184-187, 416–435.

940 Xuexin, S., Jingkai, Z., 1990. Study of fluid inclusions of the Shizhuyuan-Yejiwei W-Sn-Mo-
 941 Bi-polymetallic deposit in southern Hunan. *Mineral Deposits* 4, 004.

942 Yuan, S., Peng, J., Shen, N., Hu, R., Dai, T., 2007. ^{40}Ar - ^{39}Ar isotopic dating of the
 943 Xianghualing Sn-polymetallic orefield in southern Hunan and its geological
 944 implications. *Acta Geologica Sinica* 81, 278–286. (in Chinese with English abstract)

945 Yuan, S., Zhang, D., Shuang, Y., Du, A., Qu, W., 2012. Re-Os dating of molybdenite from
 946 the Xintianling giant tungsten-molybdenum deposit in southern Hunan province, China
 947 and its geological implications. *Acta Petrologica Sinica* 28, 27–38 (in Chinese with
 948 English abstract).

949 Yuan, S., Williams-Jones, A.E., Mao, J., Zhao, P., Yan, C., Zhang, D., 2018. The origin of the
 950 Zhangjialong tungsten deposit, South China: implications for W-Sn mineralization in
 951 large granite batholiths. *Economic Geology* 113, 1193–1208.

952 Yuan, S., Williams-Jones, A. E., Romer, R. L., Zhao, P., & Mao, J. (2019). Protolith-Related
 953 Thermal Controls on the Decoupling of Sn and W in Sn-W Metallogenic Provinces:
 954 Insights from the Nanling Region, China. *Economic Geology*, 114(5), 1005-1012.

955 Zeng, Z., Zhang, Y., Chen, Z., Chen, Y., Zhu, X., Tong, Q., Zheng, B., Zhou, Y., 2011.
 956 Geological characteristics and metallogenic epoch of pangushan W-Bi(Te) ore deposit
 957 in Yudu County, Jiangxi, Province. *Mineral Deposits* 30, 949–958. (in Chinese with
 958 English abstract)

959 Zhai, W., Sun, X., Wu, Y., Sun, H., Hua, R., Yang, Y., Li, W., Li, S., 2010. SHRIMP U-Pb
 960 zircon ages of buried granodiorite, muscovite $^{40}\text{Ar}/^{39}\text{Ar}$ mineralization age and their
 961 geological implications of Meiziwo tungsten deposit, north Guangdong Province,
 962 China. *Geological Journal of China Universities* 16, 177–185 (in Chinese with English
 963 abstract).

964 Zhai, W., Sun, X., Wu, Y., Sun, H., Hua, R., Li, W., 2011. ^{40}Ar - ^{39}Ar dating of the Yaoling
 965 tungsten deposit in the northern Guangdong Province and SHRIMP U-Pb zircon age of
 966 related granites. *Mineral Deposits* 30, 21–32. (in Chinese with English abstract)

967 Zhang, W., Hua, R., Wang, R., Chen, P., Li, H., 2007. New dating of Dajishan granite and
 968 related tungsten mineralization, South Jiangxi Province, China. *Frontiers of Earth*
 969 *Science in China* 1, 218–225.

970 Zhang, W.L., Hua, R.M., Wang, R.C., Li, H.M., Qu, W.J., Ji, J.Q., 2009. New dating of the
 971 Piaotang granite and related tungsten mineralization in Southern Jiangxi. *Acta*
 972 *Geologica Sinica* 83, 659–670.

973 Zhang, R-Q., Lu, J.-J., Wang, R-C., Yang, P., Zhu, J.-C., Yao, Y., Gao, J.-F., Li, C., Lei, Z.-
 974 H., Zhang, W.-L., Guo, W.-M., 2015. Constraints of in situ zircon and cassiterite U-Pb,
 975 molybdenite Re-Os and muscovite ^{40}Ar - ^{39}Ar ages on multiple generations of granitic
 976 magmatism and related W-Sn mineralization in the Wangxianling area, Nanling Range,
 977 South China. *Ore Geology Reviews* 65, 1021–1042.

978 Zhang, R.-Q., Lu, J.-J., Lehmann, B., Li, C., Li, G., Zhang, L., Guo, J., Sun, W., 2017.
 979 Combined zircon and cassiterite U-Pb dating of the Piaotang granite-related tungsten-tin
 980 deposit, southern Jiangxi tungsten district, China. *Ore Geology Reviews* 82, 268–284.

981 Zhao, Z., Chen, Y.C., Zeng, Z.L., Chen, Z.H., Wang, D.H., Zhao, B., Zhang, J.J., 2013.
 982 Geological characteristics and petrogenic and metallogenic ages of the Yanqian tungsten
 983 deposit in eastern Nanling region. *Jilin University. (Earth Sci. Ed.)* 43, 1828–1839. (in
 984 Chinese with English abstract)

985 Zhao, W.W., Zhou, M.F., Li, Y.H.M., Zhao, Z., Gao, J.F., 2017. Genetic types, mineralization
 986 styles, and geodynamic settings of Mesozoic tungsten deposits in South China. *Journal*
 987 *of Asian Earth Sciences* 137, 109–140.

988 Zhou, X.M., Sun, T., Shen, W.Z., Shu, L.S., Niu, Y.L., 2006. Petrogenesis of granitoids and
 989 volcanic rocks in South China: a response to tectonic evolution. *Episodes* 29, 26–33.

990 Zi, J.W., Rasmussen, B., Muhling, J.R., Fletcher, I.R., Thorne, A.M., Johnson, S.P., Cutten,
 991 H.N., Dunkley, D.J., Korhonen, F.J., 2015. In situ U–Pb geochronology of xenotime
 992 and monazite from the Abra polymetallic deposit in the Capricorn Orogen, Australia:
 993 Dating hydrothermal mineralization and fluid flow in a long-lived crustal structure.
 994 *Precambrian Research* 260, 91–112.

995
996

Figure captions

Figure 1: (A) Locations of the mining districts and ore deposits of the Cathaysia Block, South-East China. The Nanling Metallogenic Belt highlighted in orange and the southern part of the Jiangxi Province (shown in B) is outlined in red (modified and compiled from Wang and Fan, 1987; Wu et al., 1993; Jiang et al., 2006; Mao et al., 2006; Sun et al., 2012). (B) Enlargement of the southern part of the Jiangxi Province with major W deposits. The distribution of Jurassic and Cretaceous granitoids is shown in different grey tones. The Maoping deposit is located in the Dayu district and hosts the majority of the W-Sn deposits of the Nanling Metallogenic belt (modified after Huang et al., 2014; Lecumberri-Sanchez et al., 2014; Legros et al., 2016).

Figure 2: (A) Geological map and (B) simplified cross-section of the Maoping W-Sn deposit, showing the relationship between the buried peraluminous two-mica granite, the enclosing Lower Cambrian host rocks, the greisen cupola, and the W-Sn-bearing quartz veins (modified after Feng et al., 2011 and Legros et al., 2016). Sampling zone (-5 level) is shown in green.

Figure 3: Relationship between vein types and paragenetic stages in the Maoping W-Sn deposit. (A) Fe-Li-mica veins reopened and filled with Stage III W-Sn vein cross-cutting Lower Cambrian host-rock. (B) Stage III W-Sn vein, cross-cutting Stage II Fe-Li-mica vein. (C) Conjugated Stage III W-Sn veins in reopened Stage II Fe-Li-mica vein, cross-cutting and displacing the Stage I Feldspar vein. (D) Banded quartz vein showing the centimeter-scale banding of quartz and Fe-Li-mica at Stage IV. (E) Banded quartz vein

from Stage IV overprinting a previous W-Sn-topaz vein. Abbreviations accorded to IMA, Qtz: Quartz, Fe-Li-mca: Fe-Li-mica, Toz: Topaz, Wf: Wolframite.

Figure 4: Paragenetic sequence of the Maoping W-Sn deposit based on cross-cutting relationships and petrographic observations from the level -5 underground gallery (i.e. -200 m below surface; modified from Legros et al., 2016). Numbers 1 to 5 refer to the mineral generation in the overall paragenetic sequence. See text for details on the different stages, mineral abbreviations, and notations. The three types of minerals dated in this study are highlighted with an asterisk (Fe-Li-mica, wolframite and xenotime).

Figure 5: Optical and scanning electron microscope images of mica textures and mineralogical associations from the veins (stages II to IV), the greisen, and the granite. (A) Stage II feather-like centimeter-size Fe-Li-mca_{2-II} at contact to host-rock (crossed polars, transmitted light). (B) Back-scattered electron (BSE) image of homogeneous Stage II mica (Fe-Li-mca_{2-II}) with Fe-Li-ms_{1-III} and Fe-Mn hydroxides alteration along the cleavage planes. (C) Stage III Fe-Li-mca_{3-III} associated with Wf_{1-III} and Cst_{1-III} (crossed polars, transmitted light). (D) BSE image of Stage III homogeneous mica (Fe-Li-mca_{3-III}) with few Fe-Li-ms_{1-III} alteration along the cleavage planes. (E) Banded accumulation zone (see text for details) in Stage IV veins with zoned Fe-Li-mca_{4-IV} and Qtz_{4-IV} (crossed polars, transmitted light). (F) BSE image showing internal zoning and rhythmic banding between trioctahedral and dioctahedral compositions in the Fe-Li-mca_{4-IV} at Stage IV. (G) Quartz, mica, and euhedral feldspar from the granite (crossed polars, transmitted light). (H) BSE image of Fe-Li-mica from the greisen. Dark patches are the alteration of the Fe-Li-mica. (I) Quartz sub-grains, corroded mica, and altered feldspar from the granite (crossed polars, transmitted light). (J) BSE image of homogeneous Fe-Li-mica in the

Maoping granite showing rare alteration along mineral borders and micro-fractures. Abbreviations from IMA, Clb: Columbite-tantalite, Cst: Cassiterite, Fe-Li-mca: Fe-Li-mica, Mca: mica, Qtz: quartz, Ms: muscovite, Toz: topaz, Wf: Wolframite.

Figure 6: Optical and scanning electron microscope images of Stage III wolframite from the Maoping W-Sn deposit. (A) Plane-polarized transmitted light image showing complex growth zoning in wolframite associated with main Qtz_{2-III}. Note the presence of rare quartz-filled cavities (white arrows) in wolframite. (B) BSE image showing the growth zoning in wolframite and the presence of porosity and micro-cracks. (C) Patchy alteration in wolframite marked by higher Mn content and the presence of micro-inclusions of bismuthinite and cassiterite (BSE image). (D) Detail of the intense micro-porosity associated with an alteration zone (bright color) within wolframite (BSE image). Abbreviations according to IMA, Bmt: bismuthinite, Cst: cassiterite, Qtz: quartz, Wf: wolframite.

Figure 7: Distribution and mineral paragenesis associated with xenotime and fluorite in the Maoping W-Sn deposit. (A) Optical cathodoluminescence (CL) imaging of large fluorite crystal showing two distinct generations (blue and green (Fl_{2-IV}) and green (Fl_{1-IV}) colors). The different colors on CL image reflect variable trace element contents in fluorite. (B) SEM image of the core of Fl_{2-VI} characterized by heterogeneous enrichment in yttrium and infillings by REE-fluorides and xenotime. (C) SEM image of the banding zones in Fl_{2-VI} with high porosity, kaolinite, and REE minerals. Abbreviations according to IMA, Fl: fluorite, Kln: kaolinite, Xnt: xenotime, Y-Fl: yttrium-fluorite.

Figure 8: ^{40}Ar - ^{39}Ar apparent ages obtained for stage II, III, and IV Fe-Li-mica of the mineralized veins, the greisen, and the granite of the Maoping W-Sn deposit (errors reported at 2σ). Calculated ages are indicated in purple: six analyses from Stage II Fe-Li-mica at the border of the mineralized vein yield an integrated age of 157 ± 4 Ma (2σ); five samples from Stage III Fe-Li-mica associated with wolframite and cassiterite overlap within error and define an integrated age of 155 ± 4 Ma (2σ); five analyses from Stage IV Fe-Li-mica from the banded quartz veins yield an age of 158 ± 4 Ma (2σ); five samples from the greisen Fe-Li-mica (cupola at the top of the granite) define an age of 156 ± 2 Ma (2σ); seven analyses of Fe-Li-mica from the peraluminous Maoping granite overlap within error and yield an age of 156 ± 2 Ma (2σ). ^{40}Ar - ^{39}Ar isotopic data are given in Table 3.

Figure 9: Concordia diagrams for two samples (concentrate and vein) of Stage III wolframite ID-TIMS data from the Maoping W-Sn deposit. (A) and (B) full data set for both samples: (1) ore concentrate of wolframite crystals and (2) fragments of single crystal from a vein sample. Note, whether samples were selected from the concentrate or the vein, most fragments plot in two clusters on the Concordia. (C) Five fragments of the wolframite concentrate yield an age of 160.4 ± 0.4 Ma (2σ). (D) Three fragments of the wolframite vein crystals define an age of 156.3 ± 1.1 Ma (2σ). Error ellipses are shown at 2σ level. Data from Table 4.

Figure 10: $^{206}\text{Pb}/^{238}\text{U}$ vs. $^{208}\text{Pb}/^{232}\text{Th}$ Concordia diagrams for Stage VI xenotime SIMS data from the Maoping W-Sn deposit. (A) Full data set. The data straddle along the Concordia with two data clusters. (B) Nine concordant analyses overlap within error and yield an

age of 152.5 ± 1.3 Ma (2σ). (C) Nine concordant analyses overlap within error and yield an age of 130.1 ± 1.2 Ma (2σ). Error ellipses are shown at 2σ level. Data from Table 5.

Figure 11: Synthesis of geochronological data from the Maoping W-Sn deposit (this work) compared to literature data from other W-Sn vein-type deposits in the Dayu district. References: [1] Feng et al. (2011), [2] Hu et al. (2012a), [3] Zhang et al. (2017), [4] Zhang et al. (2009), [5] Deng et al. (2019), [6] Wang et al. (2016), [7] Chen et al. (2019). Dashed lines associated with the mica Ar-Ar ages represent the interval of apparent ages.

Figure 12: Compilation of available geochronological data (2σ) for W-Sn vein-type deposits in the Nanling range.

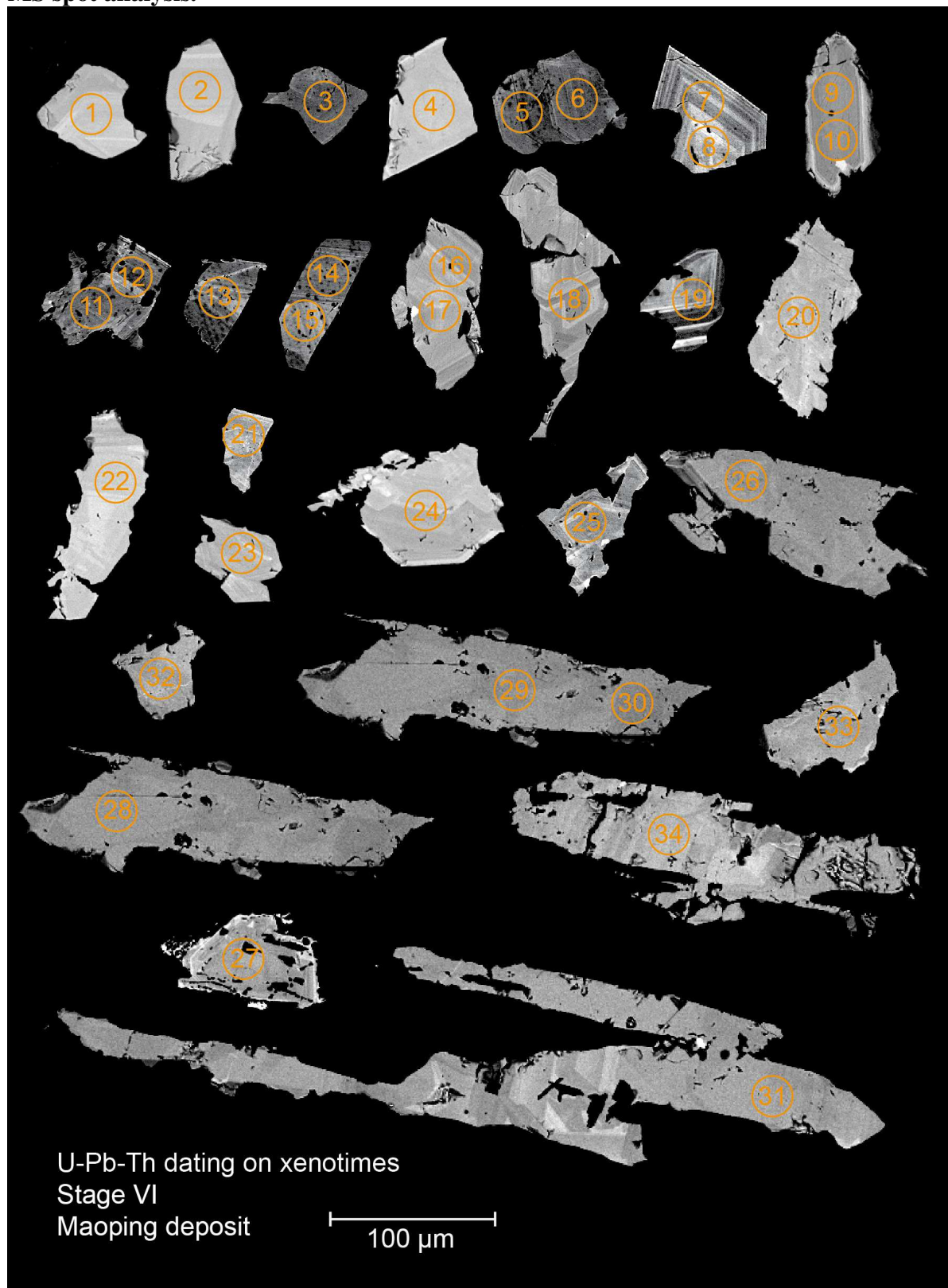
Appendix A – Detailed analytical ^{40}Ar - ^{39}Ar dating procedure on Fe-Li-mica

$^{40}\text{Ar}/^{39}\text{Ar}$ analytical work was performed at the University of Manitoba (Canada) using a multi-collector Thermo Fisher Scientific ARGUS VI mass spectrometer, linked to a stainless steel Thermo Fisher Scientific extraction/purification line, Photon Machines (55 W) Fusions 10.6 CO_2 laser, and Photon Machines (Analyte Excite) 193 nm laser. Argon isotopes (from mass 40 to 37) were measured using Faraday detectors with low noise $1 \times 10^{12} \Omega$ resistors and mass 36 was measured using a compact discrete dynode (CDD) detector. The sensitivity for argon measurements is $\sim 6.312 \times 10^{17}$ moles/fA as determined from measured aliquots of Fish Canyon Sanidine (Dazé et al., 2003; Kuiper et al., 2008). Standards and samples were placed in 2 mm deep wells in 18 mm diameter aluminium disks, with standards placed strategically so that the lateral neutron flux gradients across the disk could be evaluated. Planar regressions were fit to the standard data, and the $^{40}\text{Ar}/^{39}\text{Ar}$ neutron fluence parameter (J) interpolated for the unknowns. Uncertainties in J are estimated at 0.1 - 0.2% (1σ), based on Monte Carlo error analysis of the planar regressions (Best et al., 1995). All specimens were irradiated in the Cadmium-lined, in-core CLICIT facility of the TRIGA reactor at the Oregon State University (USA). The duration of irradiation was 17 hours. Standard used was the GA1550 biotite (Spell and McDougall, 2003). Standards for $^{40}\text{Ar}/^{39}\text{Ar}$ measurements were placed in a Cu sample tray, with a KBr cover slip, in a stainless steel chamber with a differentially pumped ZnS viewport attached to a Thermo Fisher Scientific extraction/purification line and baked with an infrared lamp for 24 hours. Single crystals were fused using the CO_2 laser. The samples selected for the $^{40}\text{Ar}/^{39}\text{Ar}$ dating were previously investigated by optical microscopy and SEM, in order to spot homogeneous areas within the analyzed minerals (mica or adularia) devoid of alteration, micro-inclusions or internal zoning. Discs of 5 mm in diameter and $\sim 150 \mu\text{m}$ thick were cut from the same polished thick section ($150 - 200 \mu\text{m}$ thick). The discs were mounted using a ceramic adhesive (PELCO) on a quartz slide placed in a stainless steel chamber with a sapphire viewport attached to the same stainless steel high vacuum extraction system as the CO_2 laser, and baked with an infrared lamp for 48 hours. For this study, a raster size of about $100 \times 100 \mu\text{m}$ was used and ablation pits were excavated to an estimated depth of $50 \mu\text{m}$. Reactive gases were removed for both the standard and unknown, after 3 minutes, by three GP-50 SAES getters (two at room temperature and one at 450°C) prior to being admitted to an ARGUS VI mass spectrometer by expansion. Five argon isotopes were measured simultaneously over a period of 6 minutes. Measured isotope abundances were corrected for extraction-line blanks, which were determined before every sample analysis. Line blanks in both the Excimer and CO_2 system averaged ~ 3 fA for mass 40 and ~ 0.013 fA for mass 36. Mass discrimination was monitored by online analysis of air pipettes based on a power law relationship (Renne et al., 2009), which gave $D = 1.0081 \pm 0.0002$ per amu, based on 71 aliquots interspersed with the unknowns. A value of 295.5 was used for the atmospheric $^{40}\text{Ar}/^{36}\text{Ar}$ ratio (Steiger and Jäger, 1977) for the purposes of routine measurement of mass spectrometer discrimination using air aliquots, and correction for atmospheric argon in the $^{40}\text{Ar}/^{39}\text{Ar}$ age calculation. Corrections are made for neutron-induced ^{40}Ar from potassium, ^{39}Ar and ^{36}Ar from calcium, and ^{36}Ar from chlorine (Roddick, 1983; Renne et al., 1998; Renne and Norman, 2001).

Appendix B – Trace element compositions of wolframite determined by LA-ICP-MS

ppm	Maoping_0		Maoping_1		Maoping_2		Maoping_3		Maoping_4	
		±		±		±		±		±
Li	3.3	0.5	2.5	0.4	2.4	0.4	2.5	0.4	2.1	0.4
Mg	10.3	0.7	6.9	0.6	6.2	0.5	5.9	0.6	13.7	0.7
Sc	169	6	135	4	189	3	367	19	209	6
Ti	18.1	2.1	16.9	2.3	9.4	1.6	8.2	1.4	21.8	2.1
V	0.4	0.1	0.2	0.1	0.1	0.1	0.1	0.0	0.3	0.1
Mn	161300	3200	120300	1400	127400	1300	175700	2000	159400	3500
Fe	37300	1400	57940	590	52430	700	26710	330	34710	770
Co	0.3	0.1	0.4	0.1	0.3	0.1	0.2	0.1	0.3	0.1
Cu	5.0	0.5	5.3	0.5	2.3	0.4	8.9	0.7	5.0	0.5
Zn	122	4	150	4	150	5	178	5	163	6
Ga	0.1	0.0	0.2	0.1	0.3	0.1	0.2	0.1	0.1	0.0
Ge	0.3	0.2	1.0	0.3	0.3	0.2	0.4	0.2	0.6	0.2
Rb	2.0	0.2	1.5	0.2	1.9	0.2	1.5	0.2	1.3	0.1
Sr	0.8	0.1	1.0	0.1	0.7	0.1	0.5	0.1	1.2	0.1
Y	166	8	192	4	185	3	65	5	59	2
Zr	43	1	84	4	132	3	31	4	27	2
Nb	3005	72	2860	49	4111	47	2260	170	1917	52
Mo	46	7	157	3	109	3	78	2	66	2
Cd	0.2	0.1	0.2	0.1	0.2	0.1	0.6	0.2	0.4	0.2
In	19	0	25	1	33	1	83	5	52	1
Sn	70	2	46	2	75	3	70	9	59	3
Hf	7.6	0.3	20.6	1.0	33.5	1.0	4.6	0.6	6.2	0.5
Ta	637	8	779	20	1127	18	1120	100	1121	47
Pb	1.1	0.2	0.6	0.1	1.4	0.2	0.9	0.1	1.0	0.1
Bi	0.8	0.1	0.3	0.0	1.2	0.2	0.4	0.1	0.9	0.1
Th	0.6	0.1	0.5	0.0	0.4	0.0	0.4	0.1	0.4	0.0
U	17.5	0.4	12.8	0.5	14.8	0.4	17.0	2.3	12.7	0.5
La	0.0	0.0	0.1	0.0	0.0	0.0	0.0	0.0	0.0	0.0
Ce	0.2	0.0	0.7	0.0	0.5	0.0	0.2	0.0	0.2	0.0
Pr	0.1	0.0	0.3	0.0	0.2	0.0	0.1	0.0	0.1	0.0
Nd	1.0	0.2	2.4	0.2	2.0	0.2	0.9	0.1	1.0	0.1
Sm	4.0	0.4	5.9	0.4	6.4	0.4	3.2	0.3	3.3	0.3
Eu	0.0	0.0	0.0	0.0	0.0	0.0	0.0	0.0	0.0	0.0
Gd	11.3	0.7	12.6	0.6	12.3	0.5	6.7	0.6	6.5	0.4
Tb	7.4	0.3	7.1	0.2	7.8	0.2	4.0	0.3	3.6	0.1
Dy	91.1	2.5	80.1	1.9	88.3	1.3	45.3	3.5	37.7	1.2
Ho	25.5	0.7	21.2	0.4	22.8	0.3	11.8	1.0	9.4	0.3
Er	118	2.5	94.4	2.2	104	1.5	55.0	4.8	39.2	1.1
Tm	34.6	0.8	27.1	0.6	30.0	0.4	16.4	1.4	10.9	0.3
Yb	391	8.8	308	6.7	345	4.0	189	16.0	119	2.9
Lu	65.4	1.5	51.6	1.0	56.9	0.6	31.5	2.7	19.1	0.5

Appendix C – Back-scattered electron images of xenotime extracted from Stage VI fluorite of the Maoping deposit. Circles indicate the location of the U-Th-Pb LA-ICP-MS spot analysis.

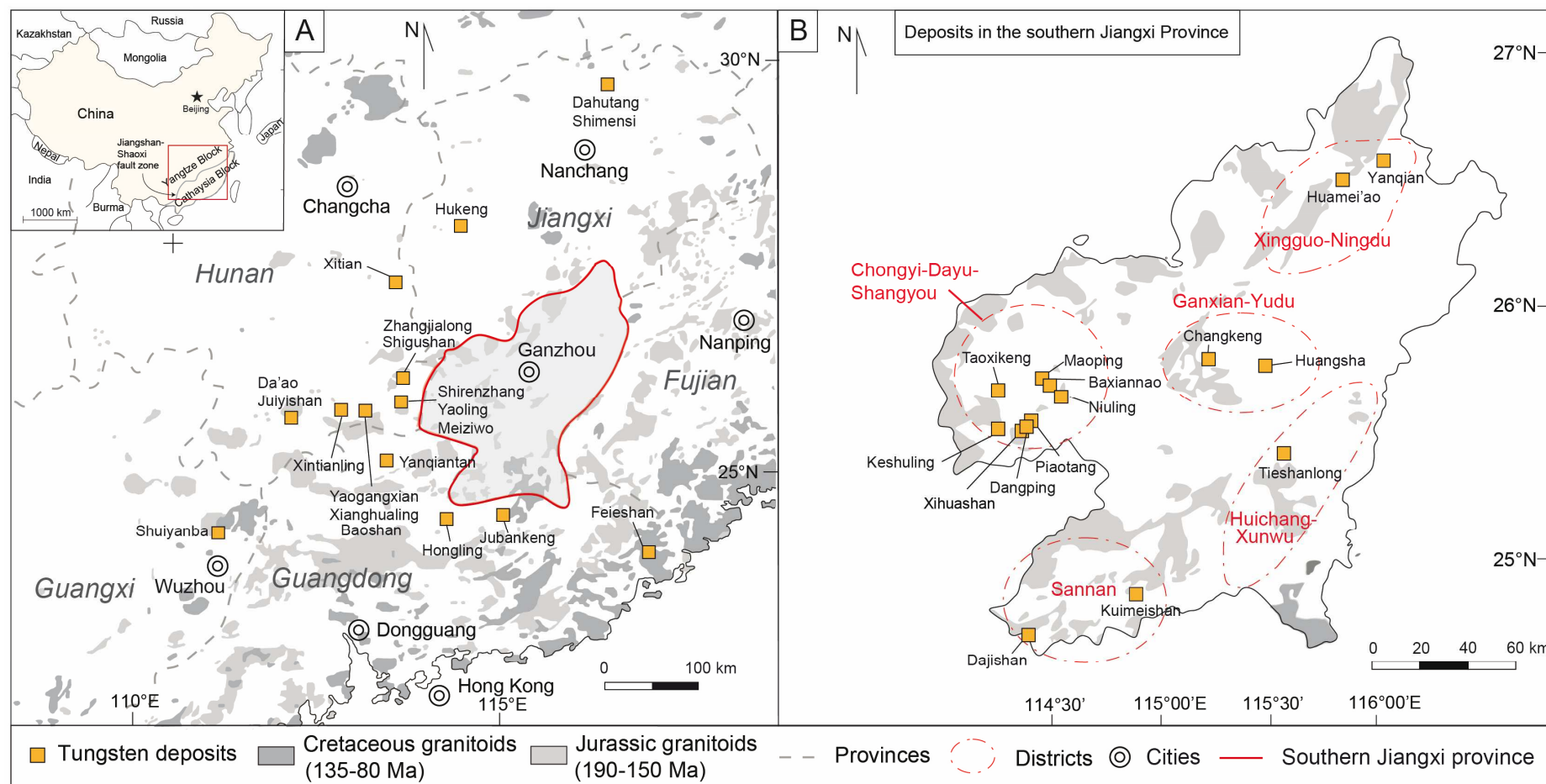


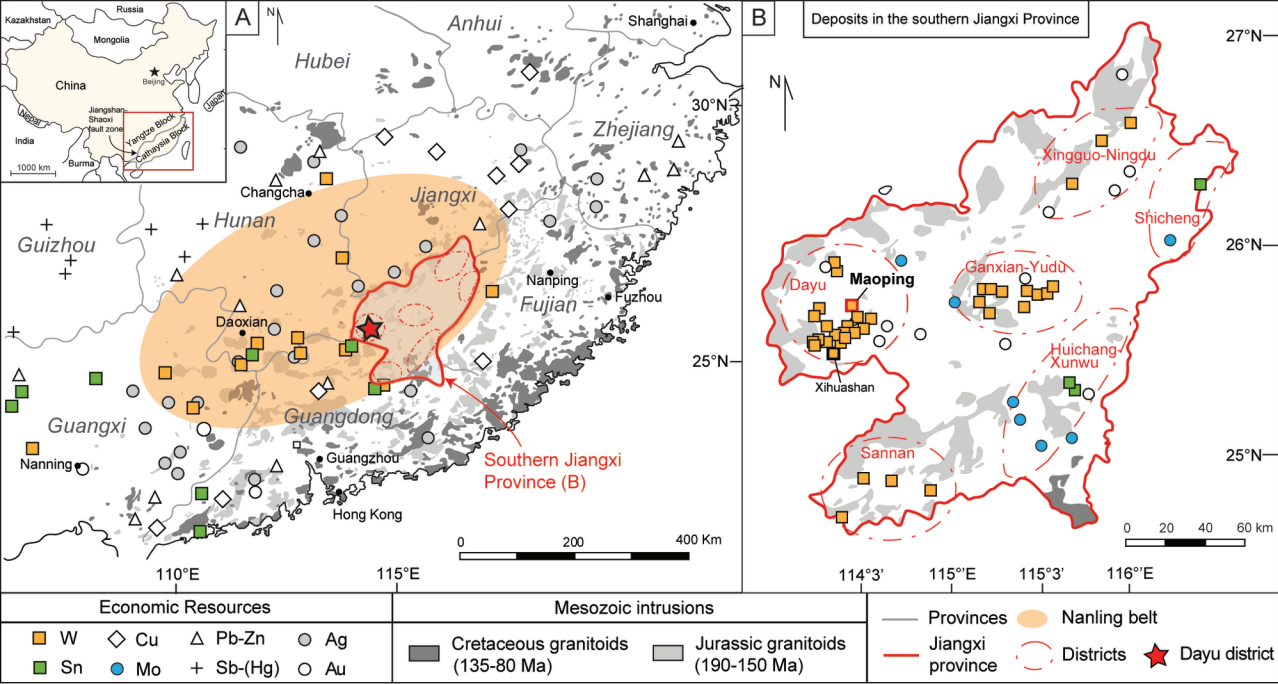
Appendix D – Compilation of geochronological data from the literature on W-Sn vein-type deposits in the Cathaysia

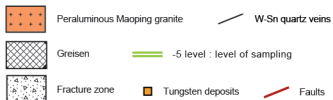
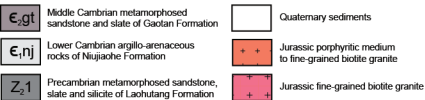
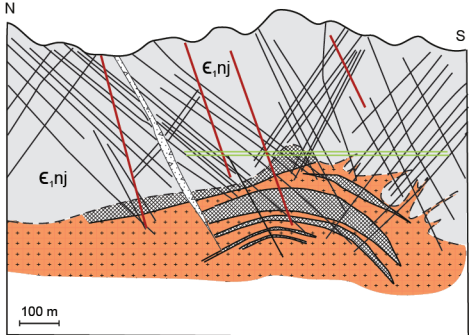
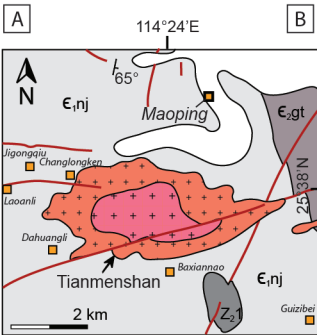
Province	Deposit	Age	2σ	Analytical method	Reference
Guangdong	Feie'shan	135.1	0.8	⁴⁰ Ar- ³⁹ Ar on mica	Liu et al., 2017
		140.6	1.9	Re-Os on molybdenite	Liu et al., 2017
	Hongling	159.1	1.5	Re-Os on molybdenite	Wang et al., 2010b
	Jubankeng	138.5	1.5	⁴⁰ Ar- ³⁹ Ar on mica	Qi et al., 2012
	Keda	160.6	1.5	⁴⁰ Ar- ³⁹ Ar on mica	Li et al., 2011
	Shirenzhang	164	4	U-Pb on cassiterite	Jiang et al., 2018
		160	4	U-Pb on cassiterite	Jiang et al., 2018
	Yanqiantan	154.4	1.6	Re-Os on molybdenite	Liu et al., 2010
Guanxi	Shuiyanba	162.5	1.2	⁴⁰ Ar- ³⁹ Ar on mica	Li et al., 2011
Hunan	Baoshan	164.2	2.6	Re-Os on molybdenite	Zhao et al., 2017
	Dao	151.3	2.4	Re-Os on molybdenite	Fu et al., 2007
	Jiuyishan	151.3	2.4	Re-Os on molybdenite	Fu et al., 2007
	Meiziwo	157.7	2.8	Re-Os on molybdenite	Qi et al., 2012
		155.9	0.6	⁴⁰ Ar- ³⁹ Ar on mica	Zhai et al., 2010
	Shigushan	154.2	2.7	Re-Os on molybdenite	Fu et al., 2008
	Shirenzhang	159.1	2.2	Re-Os on molybdenite	Fu et al., 2008
	Xianghualing	154.4	1.1	⁴⁰ Ar- ³⁹ Ar on mica	Yuan et al., 2007
		158.7	1.2	⁴⁰ Ar- ³⁹ Ar on mica	Yuan et al., 2007
		161.3	1.1	⁴⁰ Ar- ³⁹ Ar on mica	Yuan et al., 2007
	Xintianling	161.7	9.3	Re-Os on molybdenite	Yuan et al., 2012
	Xitian	149.7	0.9	Re-Os on molybdenite	Liang et al., 2016
	Yaogangxian	133.7	2.6	U-Pb hydrothermal zircon	Wang et al., 2016
		153.0	1.1	⁴⁰ Ar- ³⁹ Ar on mica	Peng et al., 2006
		154.9	2.6	Re-Os on molybdenite	Peng et al., 2006
		155.1	1.1	⁴⁰ Ar- ³⁹ Ar on mica	Peng et al., 2006
		159.1	2.0	U-Pb on wolframite	Deng et al., 2019
		153.7	0.7	U-Pb on wolframite	Deng et al., 2019
	Yaoling	159.5	2.8	Re-Os on molybdenite	Qi et al., 2012
		149.4	0.7	⁴⁰ Ar- ³⁹ Ar on mica	Zhai et al., 2011
	Zhangjialong	160.2	2.2	Re-Os on molybdenite	Yuan et al., 2018
Jiangxi	Baxiannao	157.9	1.5	Re-Os on molybdenite	Feng et al., 2011
	Changkeng	158.1	1.2	Re-Os on molybdenite	Zeng et al., 2011
	Dahutang	139.2	1.0	Re-Os on molybdenite	Mao et al., 2013
	Dajishan	147.2	1.2	⁴⁰ Ar- ³⁹ Ar on mica	Zhang et al., 2007
	Dangping	133.6	2.0	U-Pb hydrothermal zircon	Wang et al., 2016
	Huamei'ao	158.5	3.3	Re-Os on molybdenite	Feng et al., 2015
	Huangsha	153.0	3.0	Re-Os on molybdenite	Huang et al., 2011

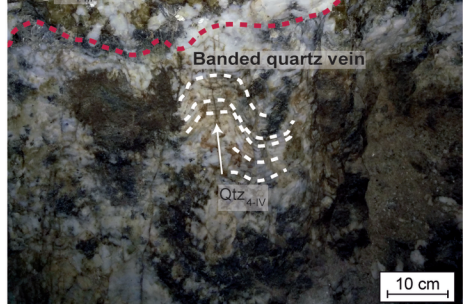
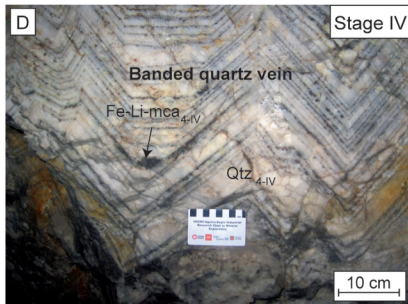
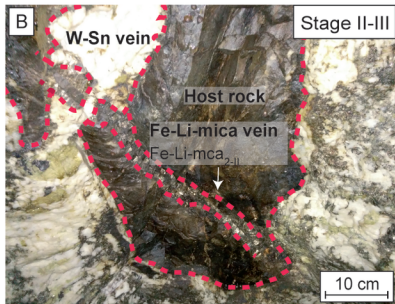
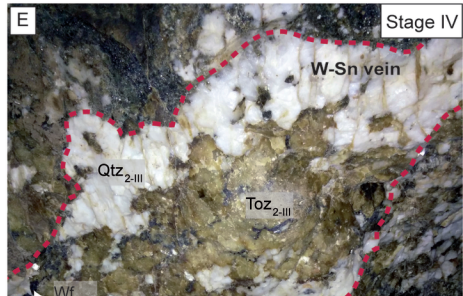
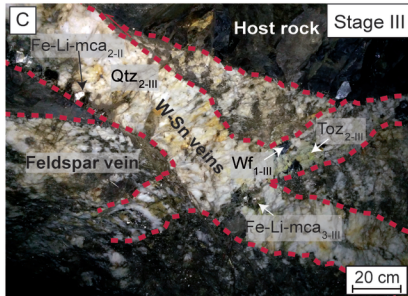
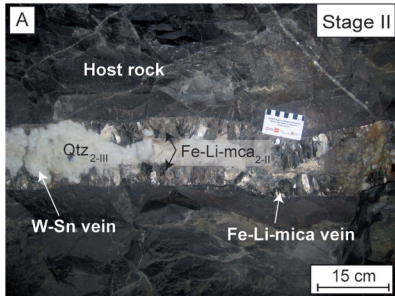
	132.9	3	U-Pb hydrothermal zircon	Wang et al., 2016
Hukeng	147.2	1.4	^{40}Ar - ^{39}Ar on mica	Liu et al., 2011
	150.2	2.2	Re-Os on molybdenite	Liu et al., 2011
Keshuling	158.8	1.2	^{40}Ar - ^{39}Ar on mica	Liu et al., 2008
Kuimeishan	153.7	1.5	Re-Os on molybdenite	Li et al., 2014
Maoping	150.2	2.8	Re-Os on molybdenite	Feng et al., 2011
	156.8	1.5	U-Pb on cassiterite	Chen et al., 2019
Niuling	154.9	4.1	Re-Os on molybdenite	Feng et al., 2011
Piaotang	152.0	1.9	^{40}Ar - ^{39}Ar on mica	Zhang et al., 2009
	159.5	1.5	U-Pb on cassiterite	Zhang et al., 2017
	159.5	1.3	U-Pb on wolframite	Deng et al., 2019
	152.1	0.9	U-Pb on wolframite	Deng et al., 2019
Shimensi	145.7	0.9	^{40}Ar - ^{39}Ar on mica	Wei et al., 2017
Taoxikeng	134.4	3.8	U-Pb hydrothermal zircon	Wang et al., 2016
	152.7	1.5	^{40}Ar - ^{39}Ar on mica	Guo et al., 2011
	153.4	1.3	^{40}Ar - ^{39}Ar on mica	Guo et al., 2011
	154.4	3.8	Re-Os on molybdenite	Guo et al., 2011
	134.2	3.2	U-Pb hydrothermal zircon	Wang et al., 2016
Tieshanlong	152.8	1.6	^{40}Ar - ^{39}Ar on mica	Hu et al., 2012a
	157.8	0.9	Re-Os on molybdenite	Hu et al., 2012a
Yanqian	159.2	2.3	Re-Os on molybdenite	Zhao et al., 2013
Zhangdou	149.1	7.1	Re-Os on molybdenite	Feng et al., 2011

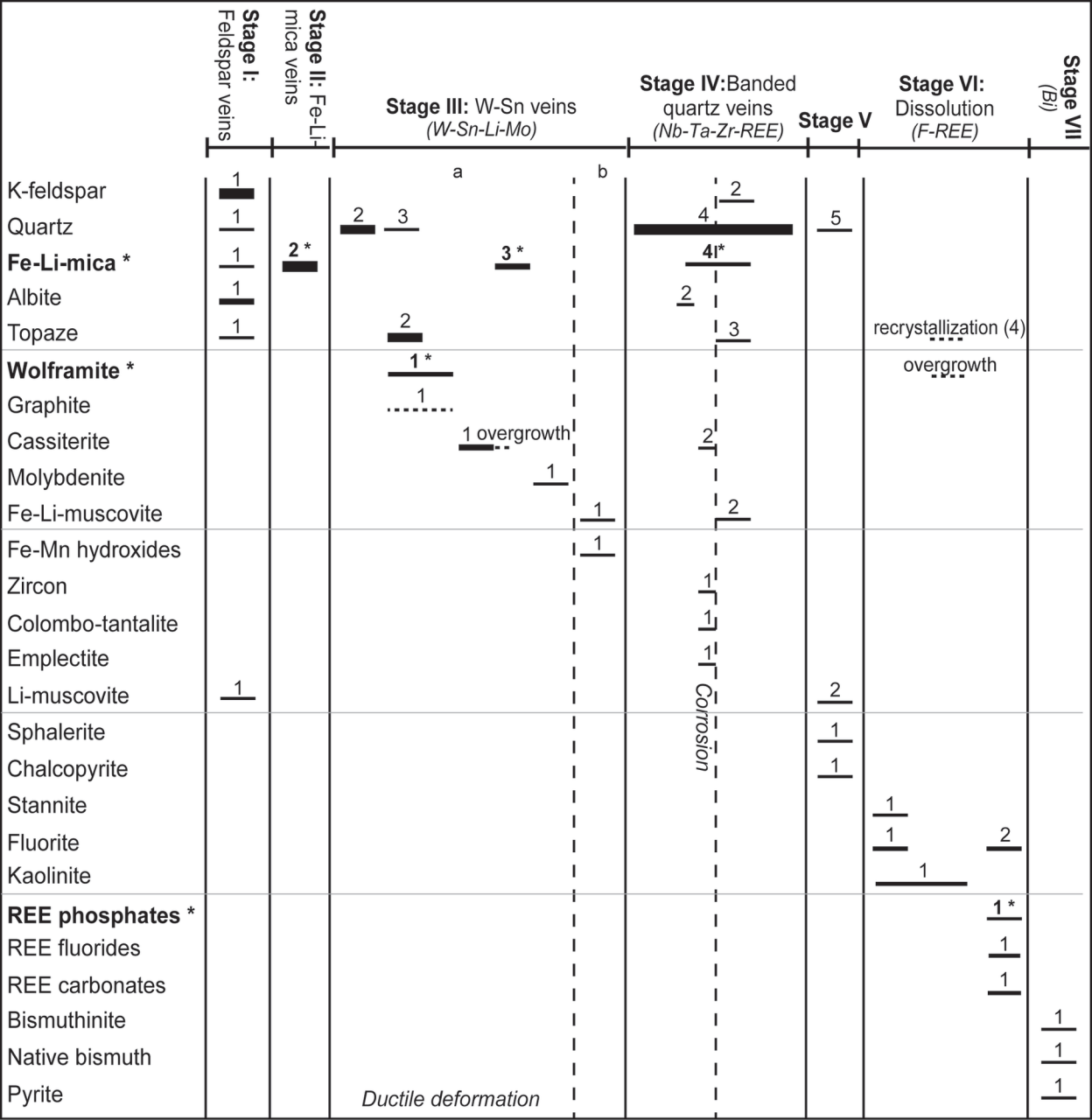
Appendix E – Map of the W-Sn vein-type deposits in the Cathaysia that have been dated (details in Appendix D and Fig. 12)

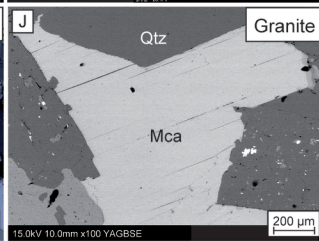
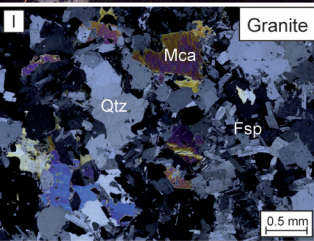
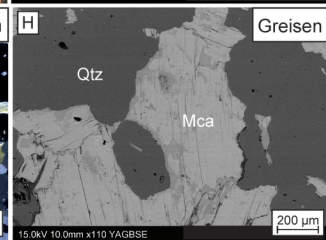
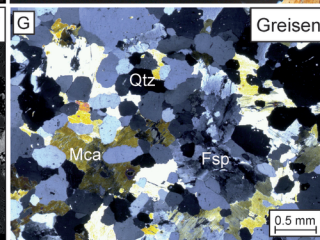
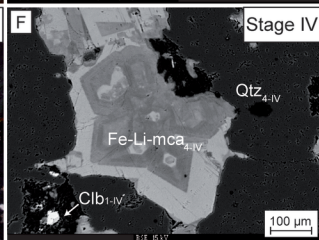
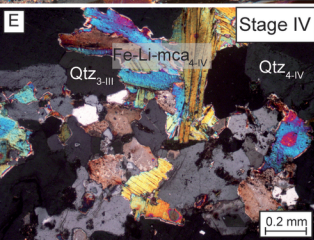
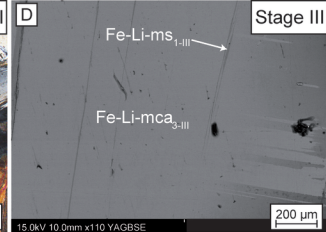
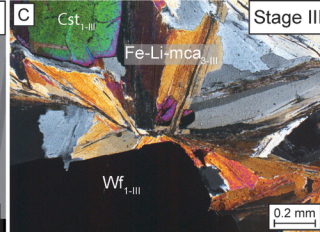
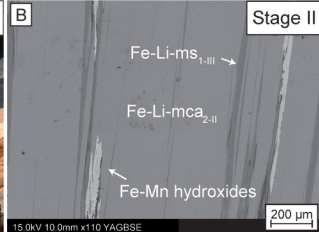
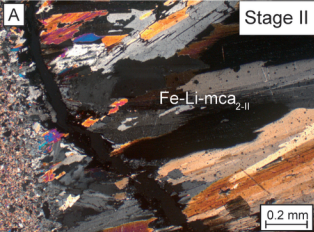


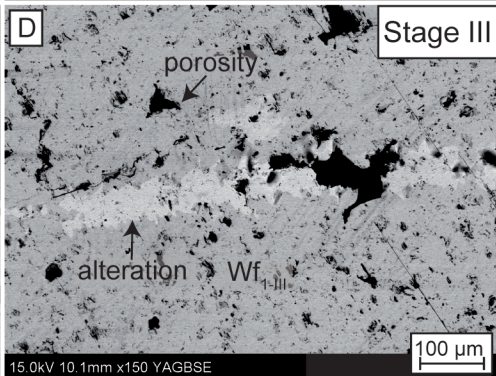
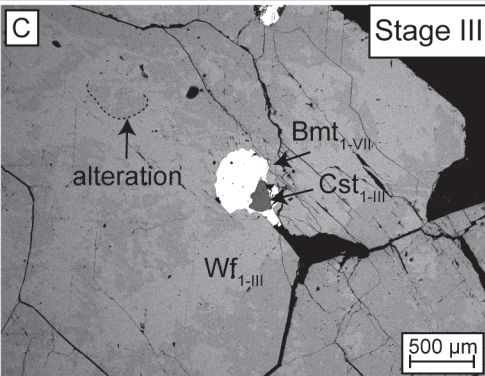
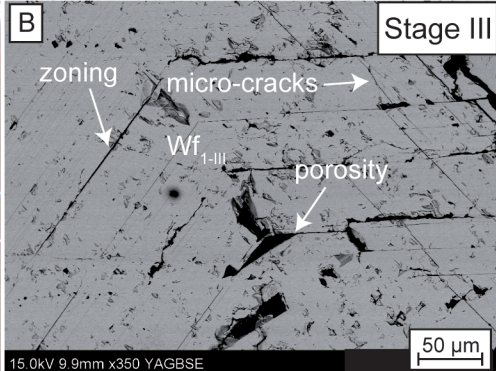
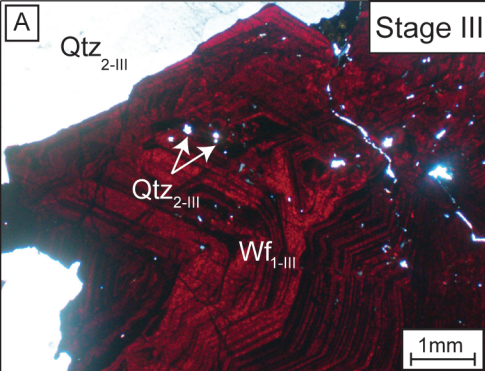






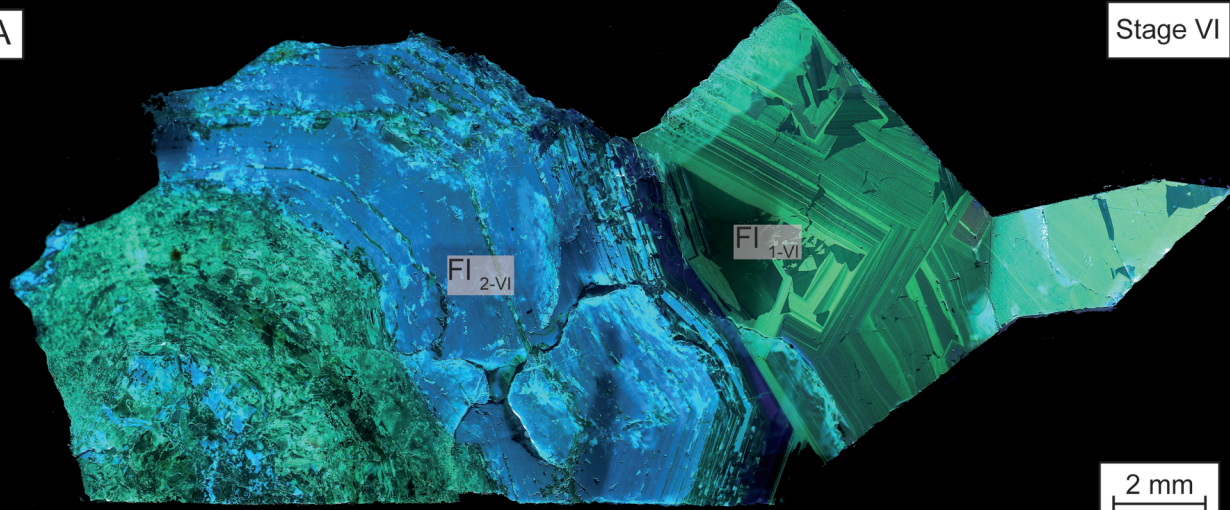






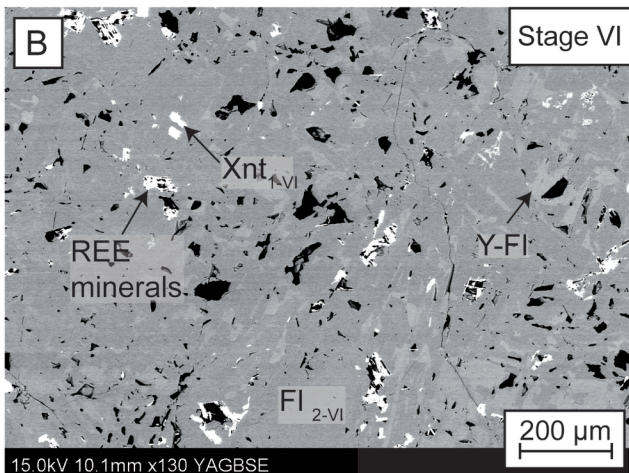
A

Stage VI



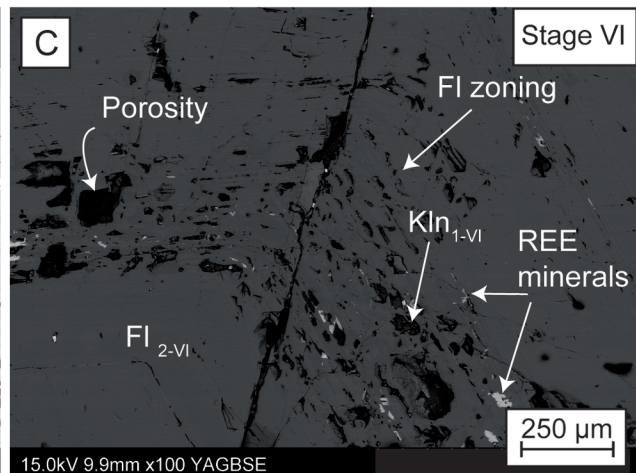
B

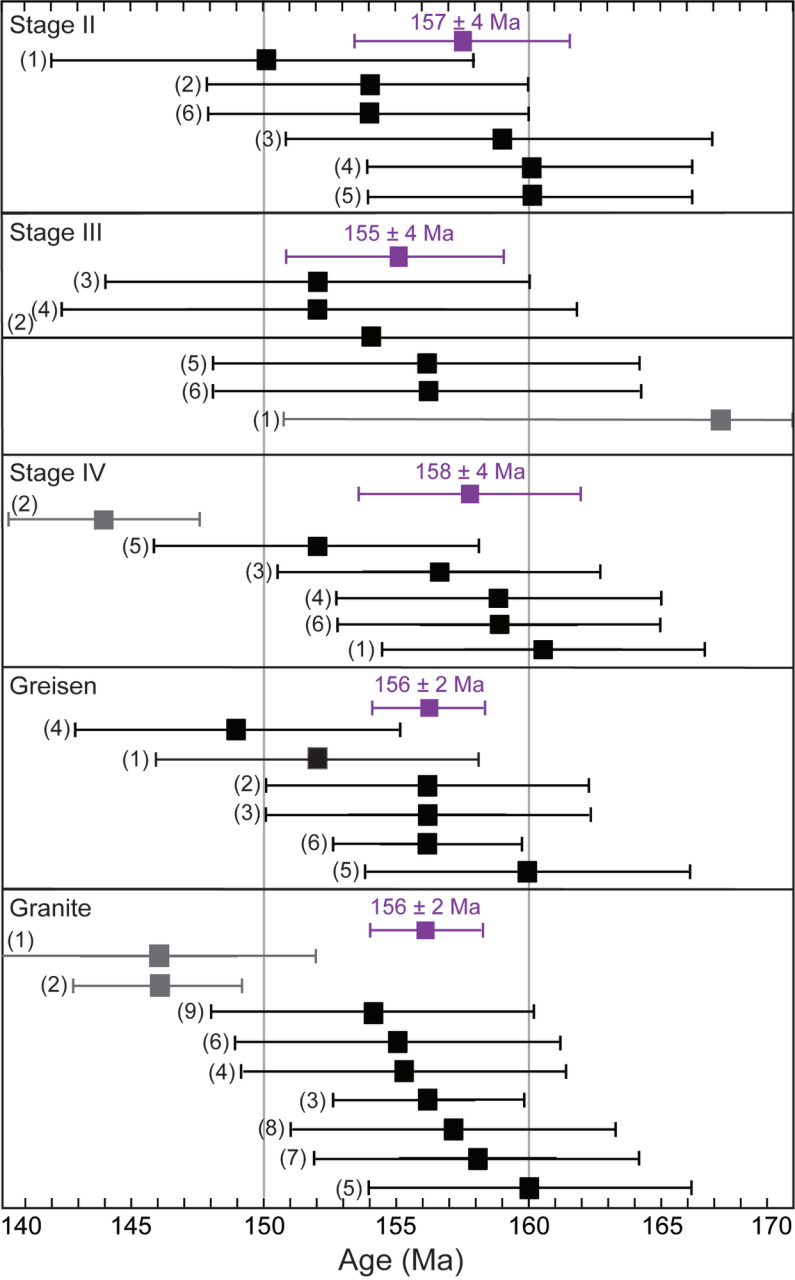
Stage VI

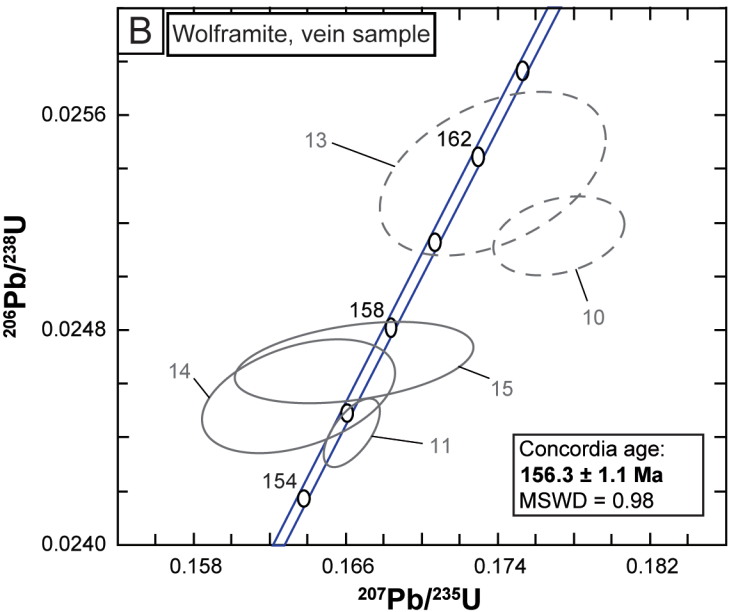
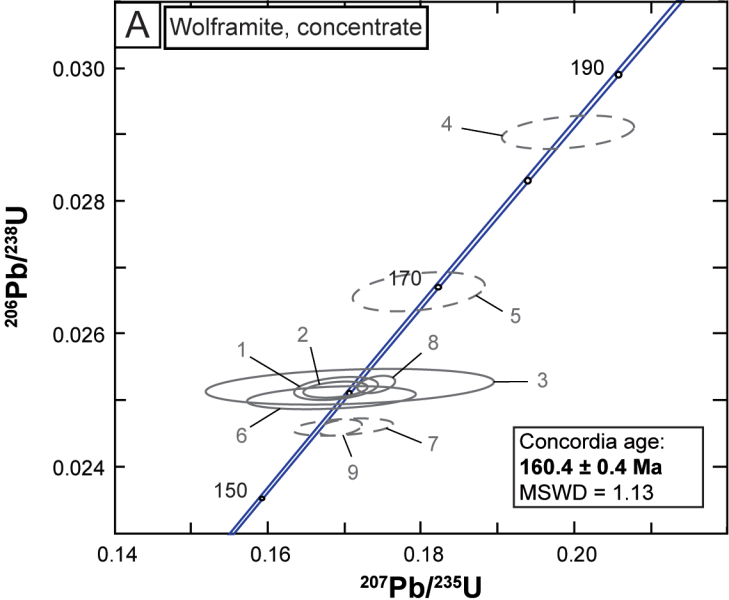


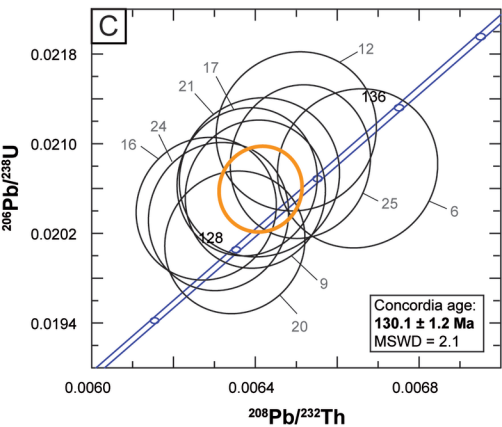
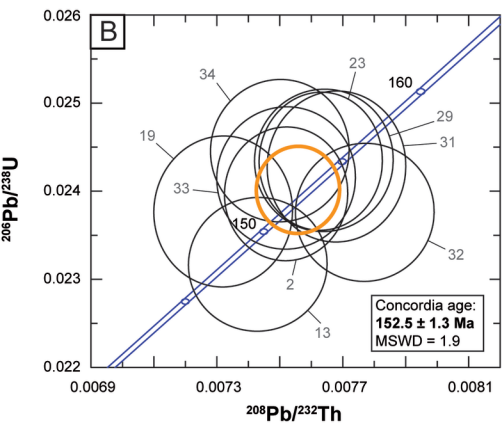
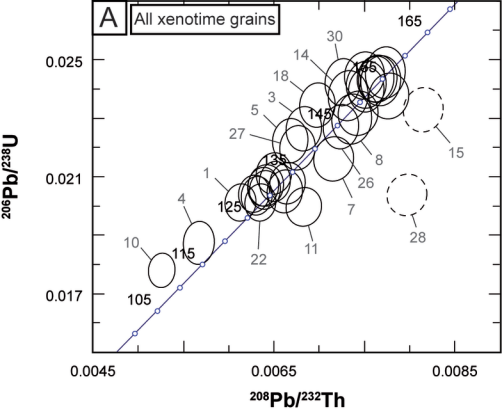
C

Stage VI



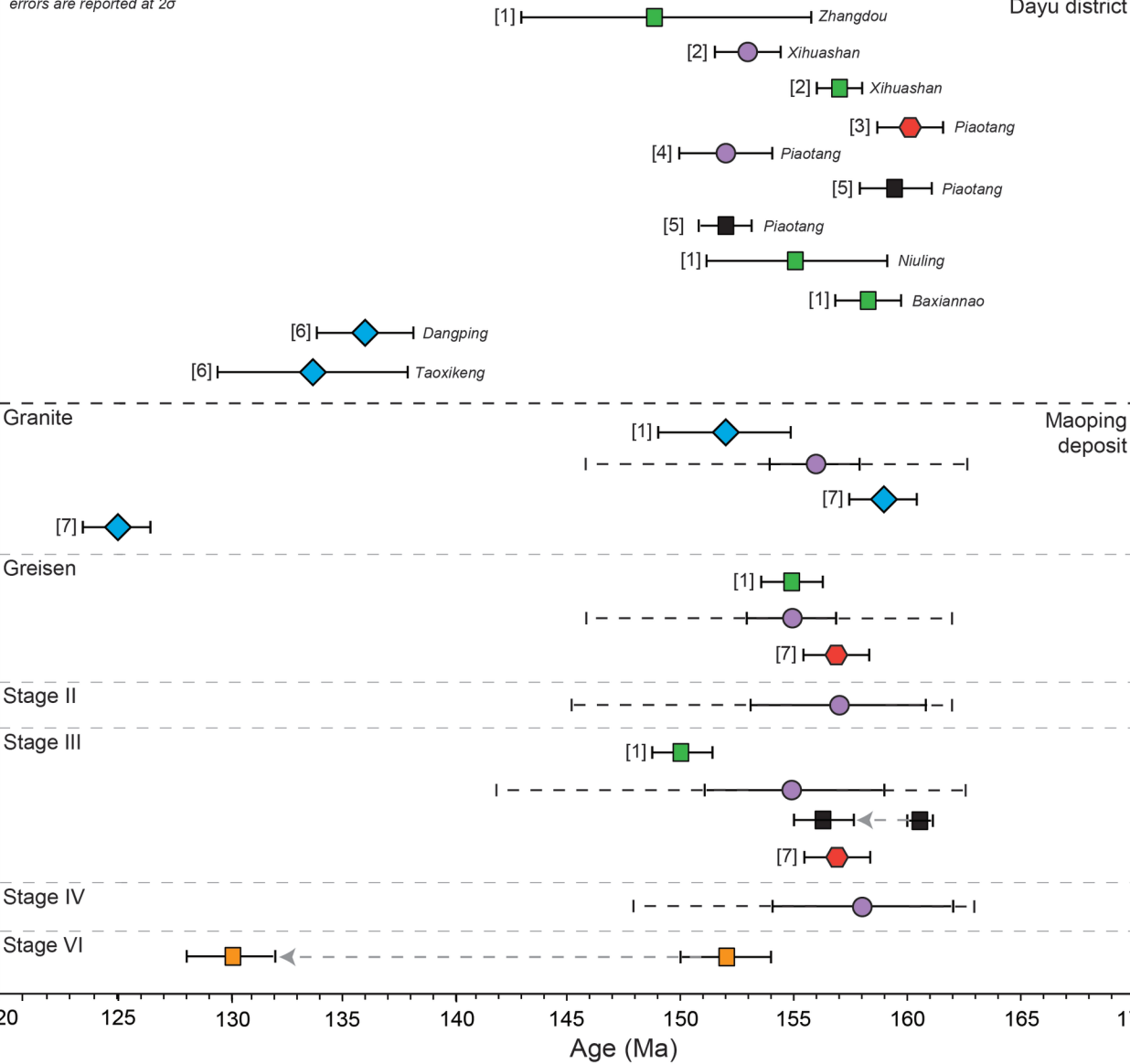




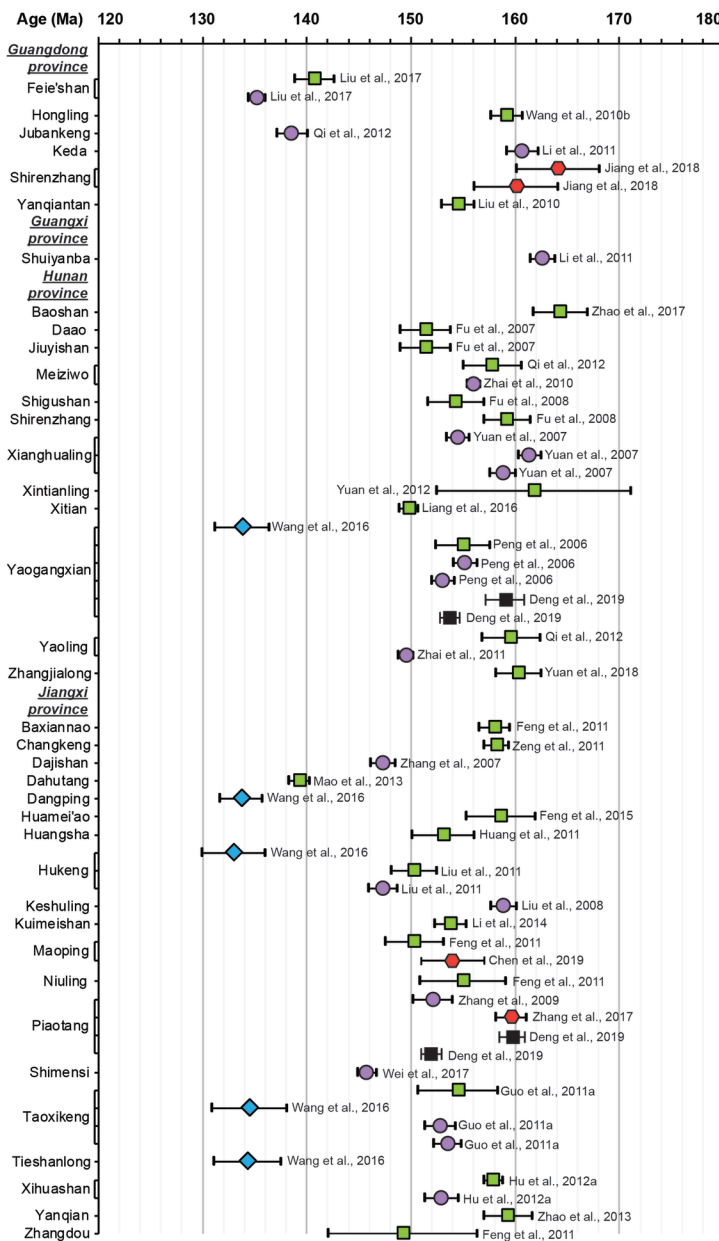


errors are reported at 2σ

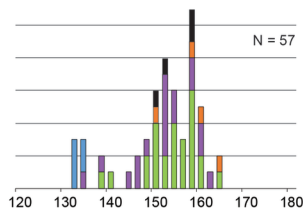
Dayu district



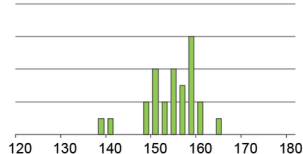
U-Pb on zircon U-Pb on wolframite U-Pb or Ar-Ar on cassiterite U-Pb on xenotime Re-Os on molybdenite Ar-Ar on micas



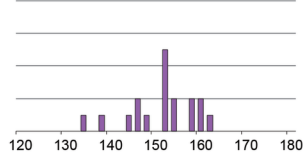
Vein dating in the Nanling Range
errors are reported at 2σ



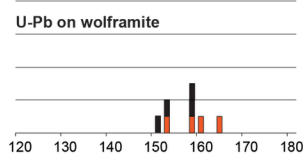
Re-Os on molybdenite N = 26



Ar-Ar on mica N = 18



U-Pb on cassiterite N = 8



U-Pb on wolframite

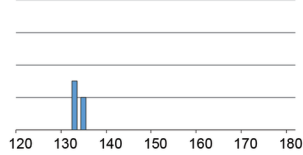


Table 1 - EMPA analyses of wolframite samples. Values preceded by the "<" symbol are below the detection limit. SD stands for Standard Deviation.

Wt.%	WO ₃	SD	MnO	SD	FeO	SD	Nb ₂ O ₅	SD	Ta ₂ O ₅	SD	Total
MP-1	76.0	2.9	17.6	0.7	7.4	0.5	0.6	0.9	<0.5	1.8	101.5
MP-2	76.8	2.9	17.1	0.7	7.1	0.5	0.5	0.8	<0.5	1.8	101.5
MP-3	75.2	2.9	17.6	0.7	7.1	0.5	0.7	0.9	1.1	1.8	101.7
MP-4	76.1	2.9	17.8	0.7	7.2	0.5	0.5	0.9	0.6	1.7	102.1
MP-5	75.4	2.9	18.0	0.8	7.1	0.5	0.8	0.8	<0.5	0.0	101.3
MP-6	76.1	2.9	18.1	0.8	6.6	0.5	<0.5	0.9	<0.5	0.0	100.8
MP-7	73.7	2.9	17.6	0.7	6.9	0.5	1.0	0.9	0.5	1.8	99.6
MP-8	76.7	2.9	17.9	0.7	7.0	0.5	0.5	0.9	<0.5	0.0	102.1
MP-9	75.6	2.9	17.8	0.8	7.0	0.5	<0.5	0.9	<0.5	0.0	100.4
MP-10	75.5	2.9	17.4	0.7	6.8	0.5	0.5	0.9	<0.5	1.8	100.3
MP-11	75.4	2.9	17.9	0.8	6.8	0.5	0.6	0.9	<0.5	1.8	100.6
MP-12	75.9	2.9	17.7	0.7	6.9	0.5	0.5	0.8	<0.5	0.0	100.9
MP-13	76.7	2.9	16.3	0.7	7.5	0.5	0.9	0.9	<0.5	1.8	101.4
MP-14	75.7	2.9	17.5	0.7	6.8	0.5	0.6	0.8	0.8	1.8	101.4
MP-15	74.7	2.9	17.0	0.7	7.2	0.5	1.1	0.9	<0.5	1.9	99.9
MP-16	77.0	2.9	17.5	0.7	7.3	0.5	<0.5	0.9	<0.5	0.0	101.8
MP-17	77.9	2.9	17.4	0.7	7.2	0.5	<0.5	0.7	<0.5	0.0	102.4
MP-18	77.6	2.9	16.8	0.7	7.2	0.5	<0.5	0.8	<0.5	0.0	101.5
MP-19	74.0	2.9	17.2	0.7	7.4	0.5	1.1	0.9	<0.5	1.9	99.7
MP-20	75.7	2.9	17.5	0.7	7.0	0.5	0.7	0.9	<0.5	0.0	100.9

Table 2 – EMPA analyses of xenotime samples. Values preceded by the "<" symbol are below the detection limit. SD stands for Standard deviation.

	34-1	SD	34-a	SD	36-a	SD	36-b	SD	24-a	SD	24-c	SD	24-e	SD	16-b-c	SD	16-b-b	SD	18-a	SD	7-a	SD	2-b	SD	8-c	SD	8-b	SD	13-a	SD	3-b	SD	5	SD	18-c	SD	18-b	SD	23	SD	28-b	SD
P ₂ O ₅	36.07	1.56	36.84	1.56	35.84	1.51	37.36	1.56	36.82	1.56	36.29	1.56	34.71	1.51	37.09	1.56	32.27	1.42	32.92	1.42	30.55	1.37	31.27	1.37	35.66	1.51	28.07	1.28	35.46	1.51	35.29	1.51	35.42	1.51	33.94	1.47	27.09	1.24	31.97	1.42	30.06	1.37
CaO	0.35	0.10	0.10	0.08	0.36	0.10	<0.1	0.10	0.69	0.11	0.66	0.11	0.19	0.10	4.46	0.25	0.60	0.10	0.36	0.10	0.26	0.10	0.35	0.10	0.31	0.10	10.14	0.42	0.46	0.10	0.96	0.13	0.25	0.10	0.59	0.11	13.54	0.52	10.90	0.45	1.80	0.15
Y ₂ O ₃	42.06	1.80	43.60	1.83	41.24	1.78	42.98	1.83	37.32	1.65	39.88	1.73	40.21	1.75	35.45	1.60	41.34	1.78	39.48	1.73	43.96	1.85	42.85	1.80	39.67	1.73	34.90	1.57	34.78	1.57	37.41	1.68	39.04	1.70	38.25	1.70	32.57	1.52	30.01	1.45	37.17	1.65
La ₂ O ₃	<0.2	0.00	<0.2	1.04	<0.2	1.00	<0.2	0.00	<0.2	1.00	<0.2	1.04	<0.2	0.00	<0.2	1.04	<0.2	1.00	<0.2	0.00	<0.2	0.00	<0.2	0.00	<0.2	0.00	<0.2	0.00	<0.2	0.00	<0.2	0.00	<0.2	1.00	<0.2	0.00	<0.2	1.00	<0.2	0.00	<0.2	0.00
Ce ₂ O ₃	<0.2	0.47	<0.2	0.00	<0.2	0.45	<0.2	0.47	<0.2	0.47	<0.2	0.00	<0.2	0.00	<0.2	0.47	<0.2	0.02	<0.2	0.47	<0.2	0.45	<0.2	0.00	<0.2	0.00	<0.2	0.00	<0.2	0.45	<0.2	0.00	<0.2	0.00	<0.2	0.00	<0.2	0.49	<0.2	0.00	<0.2	0.00
Nd ₂ O ₃	0.68	1.42	0.59	1.38	0.66	1.45	<0.4	1.35	<0.4	0.00	<0.4	1.40	<0.4	0.00	<0.4	1.59	<0.4	0.00	<0.4	0.00	<0.4	0.00	<0.4	1.28	<0.4	0.00	<0.4	1.26	0.45	1.52	<0.4	1.40	<0.4	1.26	<0.4	1.45	0.72	1.38	0.50	1.31	<0.4	1.38
Sm ₂ O ₃	1.64	0.95	0.76	0.95	1.45	0.99	0.84	0.99	0.81	0.98	1.54	1.06	0.55	0.87	1.99	1.06	0.56	0.86	0.80	1.02	<0.5	0.00	<0.5	0.84	0.94	0.88	0.54	0.86	1.68	0.99	0.92	0.91	0.89	0.98	<0.5	0.95	<0.5	0.99	<0.5	1.02	<0.5	0.90
Gd ₂ O ₃	5.85	2.19	4.62	2.08	5.16	2.17	4.32	2.19	5.25	2.19	5.09	2.28	4.07	2.10	5.87	2.35	4.12	2.14	6.13	2.40	3.90	2.03	3.55	2.14	4.75	2.05	4.29	2.03	5.63	2.31	5.65	2.31	5.58	2.31	6.36	2.31	4.33	2.05	4.74	2.21	2.59	1.84
Pr ₂ O ₃	0.32	1.31	<0.2	1.40	<0.2	1.29	0.23	1.31	0.68	1.36	0.27	1.26	<0.2	1.40	0.63	1.24	0.35	1.31	0.55	1.40	0.33	1.33	<0.2	1.31	0.33	1.33	<0.2	1.17	0.38	1.59	0.45	1.33	0.20	1.50	0.26	1.17	0.38	1.17	0.36	1.31	0.52	1.31
Dy ₂ O ₃	7.08	1.84	5.81	1.68	7.01	1.81	6.26	1.70	9.34	2.11	7.98	1.95	7.78	1.91	8.22	2.04	7.82	1.95	8.49	2.02	6.73	1.79	6.63	1.79	8.20	1.97	6.68	1.72	8.68	2.04	9.25	2.11	9.58	2.11	9.68	2.16	7.48	1.91	7.93	1.95	4.50	1.47
Er ₂ O ₃	3.46	1.40	3.72	1.40	3.97	1.49	4.02	1.53	4.58	1.46	3.99	1.46	4.48	1.51	3.89	1.46	5.11	1.53	4.02	1.44	4.61	1.51	3.89	1.51	3.76	1.42	4.36	1.44	3.79	1.51	4.56	1.56	4.09	1.53	4.02	1.56	3.68	1.40	3.51	1.37	5.18	1.53
Yb ₂ O ₃	4.03	1.46	4.90	1.57	4.03	1.55	4.18	1.55	5.04	1.53	4.87	1.62	5.28	1.66	4.01	1.55	5.11	1.66	4.08	1.50	5.27	1.66	5.77	1.64	4.45	1.57	5.46	1.62	4.63	1.59	5.42	1.59	4.91	1.64	4.73	1.62	4.51	1.59	4.10	1.46	11.44	2.14
Total	101.5		100.9		99.7		100.2		100.5		100.6		97.3		101.6		97.3		96.8		95.6		94.3		98.1		94.4		95.9		99.9		100.0		97.8		94.3		94.0		93.3	

Table 3 – ^{40}Ar - ^{39}Ar analytical data for Fe-Li-mica from Stages II, III and IV, greisen, and granite from the Maoping deposit.

Samples	Relative isotopic abundances (fAmps)*														⁴⁰ Ar*/ ³⁹ Ar(K)	⁴⁰ Ar* (%)	Apparent age		MSWD
	⁴⁰ Ar	±	³⁹ Ar	±	³⁸ Ar	±	³⁷ Ar	±	³⁶ Ar	±	Ca/K	±	Cl/K	±			Age (Ma)	± (Ma)	
	(1s)		(1s)		(1s)		(1s)		(1s)		(1s)		(1s)		(1s)		(1s)		
Stage II Fe-Li-mica																			
Spot 1	47.877	0.069	2.397	0.063	0.056	0.03	0.036	0.028	0.003	0.001	0.509	0.397	0.032	0.037	19.536	0.541	97.917	150.3	4
Spot 2	52.734	0.060	2.477	0.062	-0.024	0.028	-0.03	0.027	0.01	0.001	-0.41	0.38	-0.066	0.034	20.009	0.536	94.134	153.8	3
Spot 3	53.542	0.066	2.392	0.063	0.059	0.028	-0.008	0.026	0.013	0.001	-0.121	0.378	0.033	0.034	20.69	0.573	92.571	158.9	4
Spot 4	65.411	0.071	3.056	0.061	0.041	0.03	0.068	0.027	0.005	0.001	0.749	0.308	0.002	0.029	20.907	0.443	97.761	160.4	3
Spot 5	63.353	0.068	3.055	0.068	0.047	0.027	0.001	0.026	-0.001	0.001	0.013	0.299	0.01	0.026	20.82	0.487	100.523	159.8	3
Spot 6	62.223	0.071	3.104	0.063	0.117	0.029	0.015	0.027	0.001	0.001	0.171	0.299	0.073	0.028	19.976	0.429	99.772	153.6	3
Fluence J: 0.0044501 ± 3.38E-6														Integrated age (all spots):		157	2.0	1.33	
Stage III Fe-Li-mica																			
Spot 1	27.783	0.056	1.298	0.065	0.003	0.021	-0.04	0.023	-0.002	0.001	-0.317	0.187	-0.026	0.048	21.83	1.14	102.098	166.5	8
Spot 2	22.979	0.066	1.153	0.067	0.029	0.029	0.013	0.026	-0.001	0.001	0.114	0.234	0.039	0.074	20.066	1.217	100.746	153.6	8
Spot 3	39.574	0.067	2.01	0.065	0.056	0.028	0.033	0.025	-0.001	0.001	0.165	0.127	0.046	0.041	19.841	0.669	100.838	151.9	4
Spot 4	42.619	0.072	1.876	0.061	0.029	0.028	0.006	0.027	0.017	0.001	0.036	0.151	0.004	0.045	19.902	0.691	87.689	152.3	5
Spot 5	45.513	0.067	2.195	0.064	0.033	0.03	0.033	0.028	0.002	0.001	0.153	0.131	0.008	0.04	20.403	0.624	98.493	156.0	4
Spot 6	45.251	0.063	2.221	0.065	0.059	0.031	-0.01	0.028	-0.001	0.001	-0.049	0.129	0.041	0.042	20.453	0.62	100.49	156.4	4
Fluence J: 0.0044289 ± 5.09E-6														Integrated age (spots 2-6):		155	2.0	0.74	
Stage IV Fe-Li-mica																			
Spot 1	61.006	0.065	2.861	0.06	0.035	0.03	-0.004	0.027	0.002	0.001	-0.063	0.369	0.001	0.031	21.044	0.46	98.818	161.4	3
Spot 2	64.251	0.062	3.402	0.061	0.062	0.029	-0.035	0.027	0.001	0.001	-0.390	0.305	0.017	0.025	18.721	0.354	99.254	144.3	2
Spot 3	63.802	0.074	3.117	0.061	0.042	0.030	-0.001	0.026	-0.001	0.001	-0.021	0.327	0.004	0.028	20.492	0.423	100.223	157.4	3
Spot 4	62.474	0.073	3.008	0.066	-0.002	0.030	-0.054	0.027	-0.001	0.001	-0.685	0.344	-0.037	0.029	20.834	0.479	100.450	159.9	3
Spot 5	64.886	0.066	3.170	0.062	-0.018	0.029	0.005	0.025	0.006	0.001	0.060	0.307	-0.053	0.027	19.872	0.408	97.189	152.8	3
Spot 6	67.337	0.069	3.067	0.060	0.074	0.030	0.070	0.024	0.012	0.001	0.876	0.310	0.033	0.029	20.796	0.430	94.805	159.6	3
Fluence J: 0.0044501 ± 3.38E-6														Integrated age (all spots -2):		158	2.0	1.14	
Fe-Li-mica from the greisen																			
Spot 1	67.122	0.069	3.290	0.062	0.061	0.028	0.005	0.027	0.005	0.001	0.057	0.290	0.017	0.025	19.917	0.398	97.748	152.8	3
Spot 2	65.679	0.065	3.176	0.062	0.069	0.028	-0.012	0.025	0.003	0.001	-0.136	0.281	0.027	0.026	20.357	0.417	98.554	156.1	3
Spot 3	66.738	0.072	3.168	0.068	-0.007	0.030	-0.050	0.025	0.005	0.001	-0.553	0.285	-0.043	0.028	20.458	0.463	97.252	156.8	3
Spot 4	68.029	0.070	3.291	0.065	0.047	0.030	-0.018	0.025	0.012	0.001	-0.196	0.272	0.004	0.027	19.509	0.407	94.489	149.8	3
Spot 5	63.828	0.068	2.946	0.066	0.017	0.029	-0.030	0.029	0.006	0.001	-0.360	0.357	-0.0195	0.029	21.009	0.492	97.104	160.9	3
Spot 6	68.017	0.072	3.298	0.059	0.064	0.032	0.017	0.027	0.001	0.001	0.189	0.294	0.021	0.028	20.458	0.386	99.318	156.8	2
Fluence J: 0.0044404 ± 3.38E-6														Integrated age (all spots):		156	1.0	1.70	

Fe-Li-mica from the granite																				
Spot 1	68.008	0.072	2.952	0.065	0.009	0.029	0.013	0.026	0.039	0.001	0.487	0.95	-0.033	0.029	19.040	0.463	82.775	145.9	3	
Spot 2	98.543	0.071	3.733	0.061	0.099	0.029	0.017	0.026	0.093	0.001	0.476	0.757	0.028	0.023	18.990	0.361	72.044	145.5	2	
Spot 3	67.648	0.067	3.201	0.053	-0.037	0.031	-0.017	0.025	0.007	0.001	-0.575	0.825	-0.071	0.029	20.369	0.372	96.542	155.6	2	
Spot 4	73.026	0.067	3.084	0.062	0.044	0.029	0.044	0.029	0.035	0.001	1.492	1.014	-0.000	0.028	20.295	0.454	85.806	155.1	3	
Spot 5	78.688	0.069	2.993	0.066	0.009	0.030	0.008	0.027	0.053	0.001	0.281	0.958	-0.036	0.030	21.023	0.515	80.084	160.4	3	
Spot 6	91.833	0.065	3.012	0.062	0.075	0.029	0.033	0.026	0.104	0.001	1.139	0.912	0.018	0.029	20.255	0.483	66.506	154.8	3	
Spot 7	64.393	0.066	2.968	0.062	0.037	0.029	0.057	0.025	0.011	0.001	2.034	0.933	-0.001	0.029	20.652	0.469	95.263	157.7	3	
Spot 8	77.888	0.073	3.081	0.061	0.010	0.026	-0.035	0.026	0.048	0.001	-1.228	0.928	-0.034	0.026	20.576	0.454	81.547	157.1	3	
Spot 9	72.840	0.072	3.049	0.061	0.009	0.028	0.013	0.026	0.038	0.001	0.458	0.939	-0.033	0.027	20.103	0.442	84.263	153.7	3	
Fluence J: 0.0044243 ± 4.55E-6															Integrated age (spots 3-9):			156	1.0	0.35

* Corrected for blank, mass discrimination, and radioactive decay

Sensitivity: 6.312E-17 ± 1.047E-18 (mol/fAmp)

Values in italic were not used for age calculation.

Table 4 - U-Pb analytical results (TIMS) for wolframite from the main W-Sn vein from the Maoping deposit, Jiangxi (China).

Sample ^a	Weight (mg)	Concentrations (ppm)		²⁰⁶ Pb	Common lead (pg)	Radiogenic Pb (at%) ^c			Th/U ^d	Atomic ratios ^e			Apparent ages (Ma) ^e		
		U	Pb	²⁰⁴ Pb		²⁰⁶ Pb	²⁰⁷ Pb	²⁰⁸ Pb		²⁰⁶ Pb	²⁰⁷ Pb	²⁰⁷ Pb	²⁰⁶ Pb	²⁰⁷ Pb	²⁰⁷ Pb
Measured ratios ^b				²³⁸ U	²³⁵ U	²⁰⁶ Pb	²³⁸ U	²³⁵ U	²⁰⁶ Pb						
Concentrate (common lead : ²⁰⁶ Pb/ ²⁰⁴ Pb = 18.7, ²⁰⁷ Pb/ ²⁰⁴ Pb = 15.6, ²⁰⁸ Pb/ ²⁰⁴ Pb = 38.1)															
1	0.128	17.6	0.57	190.8	27	94.71	4.60	0.69	0.0227	.02520	.16888	.04861	160	158	129
2	0.144	19.2	0.62	190.4	32	94.59	4.60	0.81	0.0267	.02517	.16881	.04863	160	158	130
3	0.119	21.9	0.78	143.7	79	94.91	4.66	0.42	0.0140	.02522	.17071	.04909	160	160	152
4	0.152	13.9	0.62	117.5	67	94.63	4.71	0.66	0.0218	.02904	.19926	.04977	184	184	184
5	0.141	20.6	0.73	168.2	54	94.61	4.63	0.76	0.0252	.02665	.17973	.04891	169	168	144
6	0.119	16.5	1.09	55.17	519	95.85	4.67	0.51	0.0170	.02506	.16829	.04871	159	158	134
7	0.093	0.21	0.74	128.1	82	94.35	4.72	0.92	0.0306	.02461	.16982	.05004	157	159	197
8	0.399	20.1	0.54	420.3	6	94.26	4.71	1.02	0.0340	.02525	.17415	.05001	161	163	196
9	0.331	19.1	1.37	266.6	15	32.49	1.62	65.89	6.3578	.02460	.16942	.04994	157	159	192
Vein sample (common lead : ²⁰⁶ Pb/ ²⁰⁴ Pb = 18.7, ²⁰⁷ Pb/ ²⁰⁴ Pb = 15.6, ²⁰⁸ Pb/ ²⁰⁴ Pb = 38.1)															
10	1.114	10.2	0.49	83.38	64	94.04	4.80	1.15	0.0384	.02515	.17722	.05110	160	166	245
11	1.029	12.2	0.32	385.6	3	94.60	4.67	0.73	0.0243	.02442	.16629	.04939	155	156	166
12	1.000	8.16	29.4	19.22	835000	f	f	f							
13	1.254	8.16	0.31	125.5	15	94.22	4.68	1.10	0.0365	.02539	.17374	.04963	162	163	178
14	1.139	8.11	0.27	156.4	8	94.86	4.58	0.56	0.0185	.02456	.16349	.04828	156	154	113
15	1.175	11.0	0.46	99.20	46	94.33	4.61	1.06	0.0352	.02468	.16643	.04890	157	156	143

a Small fragments from single wolframite grains. Fragments were selected to show only fresh fracture surfaces. Samples were washed in H₂O and acetone.

b Lead isotope ratios corrected for fractionation, blank and isotopic tracer. Samples were analyzed at GFZ German Research Centre for Geosciences, Potsdam, Germany, using a ²⁰⁵Pb-²³⁵U mixed isotopic tracer. Analytical details are given in Romer and Lüders (2006). During the measurement period total blanks were less than 15 pg for lead and less than 1 pg for uranium.

c Lead corrected for fractionation, blank, isotopic tracer, and initial lead. The initial lead isotopic composition was estimated using the intercept in the ²⁰⁶Pb/²⁰⁴Pb vs. ²³⁸U/²⁰⁴Pb diagram and correlation in the Pb isotopic composition of the wolframite sample.

d ²³²Th/²³⁸U calculated from radiogenic ²⁰⁸Pb/²⁰⁶Pb and the age of the sample.

e Apparent ages were calculated using the constants recommended by IUGS. $\lambda_{238} = 1.55125 \text{ E-10 y}^{-1}$, $\lambda_{235} = 9.848 \text{ E-10 y}^{-1}$.

f Sample dominated by common lead; measured ²⁰⁶Pb/²⁰⁴Pb = 19.22, ²⁰⁷Pb/²⁰⁴Pb = 15.67, ²⁰⁸Pb/²⁰⁴Pb = 38.79.
Data in italic were not used for age calculation.

Table 5 – U-Th-Pb analytical data (LA-ICP-MS) for xenotime from Stage VI of the Maoping deposit.

Spot#	Isotopic ratios				Measured ages			
	$^{208}\text{Pb}/^{232}\text{Th}$	1 σ	$^{206}\text{Pb}/^{238}\text{U}$	1 σ	$^{208}\text{Pb}/^{232}\text{Th}$	1 σ (Ma)	$^{206}\text{Pb}/^{238}\text{U}$	1 σ (Ma)
1	<i>0.00613</i>	<i>0.00007</i>	<i>0.02012</i>	<i>0.00026</i>	<i>123.6</i>	<i>1.36</i>	<i>128.4</i>	<i>1.67</i>
2	0.00752	0.00008	0.02397	0.00031	151.4	1.64	152.7	1.93
3	<i>0.00683</i>	<i>0.00008</i>	<i>0.02264</i>	<i>0.00031</i>	<i>137.5</i>	<i>1.57</i>	<i>144.3</i>	<i>1.98</i>
4	<i>0.00567</i>	<i>0.00007</i>	<i>0.01874</i>	<i>0.00030</i>	<i>114.3</i>	<i>1.31</i>	<i>119.7</i>	<i>1.89</i>
5	<i>0.00668</i>	<i>0.00008</i>	<i>0.02223</i>	<i>0.00031</i>	<i>134.6</i>	<i>1.54</i>	<i>141.8</i>	<i>1.96</i>
6	0.00665	0.00008	0.02078	0.00029	134.0	1.60	132.6	1.82
7	<i>0.00716</i>	<i>0.00009</i>	<i>0.02161</i>	<i>0.00031</i>	<i>144.3</i>	<i>1.77</i>	<i>137.8</i>	<i>1.99</i>
8	<i>0.00736</i>	<i>0.00009</i>	<i>0.02297</i>	<i>0.00035</i>	<i>148.3</i>	<i>1.88</i>	<i>146.4</i>	<i>2.22</i>
9	0.00662	0.00008	0.02050	0.00030	133.3	1.51	130.8	1.88
10	<i>0.00526</i>	<i>0.00006</i>	<i>0.0178</i>	<i>0.00024</i>	<i>106.0</i>	<i>1.14</i>	<i>113.8</i>	<i>1.51</i>
11	<i>0.00683</i>	<i>0.00008</i>	<i>0.01997</i>	<i>0.00027</i>	<i>137.7</i>	<i>1.65</i>	<i>127.5</i>	<i>1.69</i>
12	0.00650	0.00008	0.02111	0.00029	130.9	1.57	134.7	1.83
13	0.00743	0.00009	0.02317	0.00031	149.7	1.74	147.7	1.97
14	<i>0.00726</i>	<i>0.00008</i>	<i>0.02423</i>	<i>0.00033</i>	<i>146.3</i>	<i>1.68</i>	<i>154.3</i>	<i>2.08</i>
15	<i>0.00815</i>	<i>0.00009</i>	<i>0.02329</i>	<i>0.00031</i>	<i>164.0</i>	<i>1.90</i>	<i>148.4</i>	<i>1.96</i>
16	0.00628	0.00007	0.02042	0.00026	126.6	1.36	130.3	1.66
17	0.00638	0.00007	0.02066	0.00027	128.5	1.39	131.8	1.68
18	<i>0.00698</i>	<i>0.00008</i>	<i>0.02345</i>	<i>0.00031</i>	<i>140.6</i>	<i>1.52</i>	<i>149.4</i>	<i>1.93</i>
19	0.00732	0.00009	0.02377	0.00035	147.5	1.73	151.4	2.22
20	0.00635	0.00007	0.02012	0.00026	127.9	1.40	128.4	1.67
21	0.00641	0.00008	0.0207	0.00029	129.1	1.54	132.1	1.81
22	0.0064	0.00007	0.02055	0.00027	128.9	1.44	131.2	1.71
23	0.00763	0.00008	0.02434	0.00032	153.6	1.70	155.0	2.03
24	0.00631	0.00007	0.02035	0.00027	127.1	1.42	129.9	1.72
25	0.00651	0.00007	0.02084	0.00028	131.2	1.50	133.0	1.76
26	<i>0.00724</i>	<i>0.00008</i>	<i>0.02271</i>	<i>0.00031</i>	<i>145.9</i>	<i>1.69</i>	<i>144.8</i>	<i>1.96</i>
27	<i>0.00676</i>	<i>0.00008</i>	<i>0.02199</i>	<i>0.00031</i>	<i>136.1</i>	<i>1.54</i>	<i>140.2</i>	<i>1.93</i>
28	<i>0.00797</i>	<i>0.00009</i>	<i>0.02038</i>	<i>0.00029</i>	<i>160.5</i>	<i>1.86</i>	<i>130.0</i>	<i>1.84</i>
29	0.00764	0.00009	0.02435	0.00033	153.8	1.75	155.1	2.08
30	<i>0.00773</i>	<i>0.00009</i>	<i>0.02456</i>	<i>0.00036</i>	<i>155.6</i>	<i>1.88</i>	<i>156.4</i>	<i>2.26</i>
31	0.00768	0.00009	0.02428	0.00035	154.6	1.82	154.7	2.20
32	0.00777	0.00009	0.02376	0.00032	156.4	1.83	151.4	2.04
33	0.00752	0.00009	0.02415	0.00033	151.4	1.75	153.8	2.05
34	0.00750	0.00009	0.02446	0.00033	151.1	1.75	155.8	2.08

Data in italic were not used for age calculation.

